Electronic and optical properties of quantum dots in two-dimensional topological insulators

by

Benjamin Puzantian

A thesis submitted

in partial fulfillment of the requirements

for the Master of Science degree in Physics

Department of Physics

University of Ottawa

Ottawa-Carleton Institute of Physics

Ottawa, Canada

March 21, 2023

Abstract

This thesis presents a theoretical study of the electronic and the optical properties of quasi two-dimensional quantum dots in topological insulators. A topological insulator is a semiconductor with an insulated bulk in which electronic states, localized at the edges of the material can be found. Two-dimensional topological insulators can be described by a simple $\vec{k} \cdot \vec{p}$ model given by the Bernevig-Hughes-Zhang (BHZ) Hamiltonian.

Topological insulators have two topologically different phases: trivial and non-trivial, and can exist in one of them. We show that the trivial versus non-trivial properties of the BHZ Hamiltonian are characterized by the different topologies that arise when mapping the in-plane wavevectors through the BHZ Hamiltonian onto a Bloch sphere. In the topologically non-trivial case, edge states are formed in the nanoribbon, disc, and square quantum dot geometries. The number of states appearing in and the size of the energy gap of these quantum dots are controlled by the spatial dimensions: width W, radius R, and lateral size a, respectively. The energy spectra of these quantum dots were found by using exact diagonalization techniques. An analytical solution for the edge states with zero-energy in the bulk energy gap of the nanoribbon was derived. From this, the decay length of the edge state into the center of the quantum dot, and its position with respect to the physical edge were determined. Furthermore, the transition from the non-trivial to the trivial phase

was realized by tuning the compressive strain in the quantum dot, which resulted in the edge states disappearing from the energy gap. Thus, straining HgTe topological insulator quantum dots can be used to control the quantized spin-Hall conductance via the emergence and disappearance of edge states. These findings can be used as a design model of a quantum strain sensor based on strain-driven transitions in a HgTe quantum dot in a topological insulator.

Finally, the optical response of the bulk BHZ model to circularly polarized light was studied, yielding absorption coefficients with the strength dependent on the energy of the photons. From this study, it was found that circularly polarized light is selectively absorbed depending on the spin of the topological insulator. Building on this work may allow for an understanding of the role of edge states in optical transitions, and could enable a study of excitations in HgTe in quantum dots in topological insulators.

Acknowledgments

First and foremost, I would like to thank Dr. Pawel Harwylak for giving me the opportunity to be a graduate student in the Quantum Theorey Group, your mentorship, kindness and support, and acquaintanceship throughout these past few years have benefited me personally and professionally and has made me into a better scholar and person. Moreover, I thank Yasser Saleem for helping me get started on this project, for putting up with me, and acquaintanceship. I also would like to thank Dr. Marek Korkusinski for helping me with the theory of this project and for always being quick to help and answer my questions, day or night, no matter how potentially colorless they were. Your support and selflessness do not go unnoticed. In addition, I thank all of my colleagues in the Quantum Theory group, past and present. Special thanks to Dr. Liang Chen and Dr. Louis Gaudreau for taking the time to examine this thesis and for their stimulating questions. I would also like to thank all of the professors from the University of Ottawa during my undergraduate and graduate studies that made my time studying physics enjoyable; at times stressful, but always exciting.

To my love and my rock, Olivia Ellis, since words cannot express what you mean to me and my gratitude to you, I can only settle with thank you and I love you with all my heart.

I would also like to thank Jesse Lazare and Nikolay Izmerli for their friendships

and inspiration throughout this journey. I humbly thank my mother, Marla, for her steadfast support and encouragement throughout this endeavour and far before it. Your support and encouragement has helped shape me into the person I am today, and for that I thank you. Last but not least, I would like to acknowledge and thank my father, Allan and brothers, Shane and Jordan, for their support and for motivating me throughout these past few years.

Dedication

I dedicate this thesis to my grandfather, David Salonin, who is sadly no longer with us, but whose eccentric curiosity to understand the unknown and ingenuity undoubtedly ignited my own.

Publications

1. Puzantian B, Saleem Y, Korkusinski M, Hawrylak P. Edge States and Strain-Driven Topological Phase Transitions in Quantum Dots in Topological Insulators. Nanomaterials. 2022; 12(23):4283.

Statement of Originality

Chapters 1 and 2 of this thesis provide a review of well-known theories and models that will serve to set the stage for the thesis' contributions to the field, which are presented in Chapters 3, 4, and 5. The HgTe bandstructure's calculations in Chapter 2 were computed by Benjamin Puzantian. This was done by implementing HgTe's tight-binding parameters found in Allan et al.'s work [1] into the Quantum Theory Group's *QNANO* code under the guidance and supervision of Abdulmenaf Altintas, Marek Korkusinski, and Pawel Hawrylak. Moreover, section 2.3 of Chapter 2 is part of a paper entitled, "Edge states and strain-driven topological phase transitions in quantum dots in topological insulators" published in *Nanomaterials* [2] with Benjamin Puzantian, Yasser Saleem, Marek Korkusinski, and Pawel Hawrylak as the authors. Section 2.3 also presents a study of the topological phases of the BHZ model, which was analytically and computationally calculated by Benjamin Puzantian under the supervision of Yasser Saleem and Pawel Hawrylak.

Chapters 3 and 4 appear in the same *Nanomaterials* article. Building off of previous work on strain-driven topological phase transitions in eight-band HgTe disc quantum dots [3], this thesis presents edge states and strain-driven topological phase transitions in four-band BHZ HgTe square quantum dots. The edge states were found by using exact diagonlization techniques. First, Hamiltonian matrices of the quantum dots were derived, then this matrix was diagonlized in *Python* in order to

obtain the eigenvalues and eigenvectors. This work was done by Benjamin Puzantian under the supervision and guidance of Yasser Saleem and Pawel Hawrylak. On the other hand, the analytical and numerical calculations of the BHZ HgTe topological insulator nanoribbon and disc quantum dots were done by Marek Korkusinski, and the nanoribbon results were verified by Benjamin Puzantian and Yasser Saleem. As well, the effects of strain in the BHZ HgTe topological insulator quantum dots were studied by Benjamin Puzantian under the supervision of Marek Korkusinski.

Finally, Chapter 5 presents calculations of the absorption coefficients for the bulk BHZ model, and the interaction of an HgTe topological insulator square quantum dot with circularly polarized light. The analytical and numerical calculations were done by Benjamin Puzantian under the supervision of Yasser Saleem and Pawel Hawrylak.

Contents

List of Acronyms

0D	Zero-Dimensional
1D	One-Dimensional
2D	Two-Dimensional
3D	Three-Dimensional
BHZ	Bernevig-Hughes-Zhang
FIR	Far-Infrared
QD	Quantum Dots
QH	Quantum Hall
QSH	Quantum Spin Hall
SO	Spin-Orbit
TDSE	Time-Dependent Schrödinger Equation
TI	Topological Insulator
TISE	Time-Independent Schrödinger Equation
TRS	Time-Reversal Symmetry

List of Tables

List of Figures

Chapter 1

Introduction

The notion of an atom was first proposed by the ancient Greek philosopher Democritus around 400 BCE [4], who suggested "atomos" were tiny, indivisible, solid objects that made up matter in the universe. Today, the field of condensed matter physics is primarily concerned with the behaviour and physical properties of solids at the quantum level. A solid is simply an arrangement of atoms that form a lattice. Studying the physical properties of materials such as these solids can enhance our understanding of our world and the universe at the quantum level due to some of their exotic properties. Particularly, an interesting and relatively new class of materials, known as topological insulators (TIs), with promising possible electronic properties has emerged as of late [5, 6]. This material's electronic and optical properties will be the focus of this thesis.

1.1 Overview of topological insulators

A TI is a semiconductor with an insulated bulk and an energy gap in which the gapless helical states localized at the edge of the material, protected under time-reversal

symmetry, were predicted to exist [5–12]. Presently, there is significant interest in TIs [5–8, 10–19]. This interest was stimulated by the experimental demonstration of edge states and the spin quantum Hall effect in HgTe/CdTe quantum wells with an inverted band structure [8] and in other materials [6, 10–12, 16, 17, 19–23]. Moreover, the enthusiasm in TIs is also motivated by HgTe-based nanocrystals and nanoplatelets [24, 25] as potential applications for far-infrared (FIR) detectors [26, 27].

The theory of interface between non-trivial (topological) and trivial (normal) HgTe insulators was pioneered by Volkov and Pankratov [7], and significantly developed by Zhang et al. [5] and Fu and Kane [28]. Zhang et al. [5] used the $\vec{k} \cdot \vec{p}$ theory to derive the four-band effective 2D (BHZ) Hamiltonian. The BHZ Hamiltonian is one of the simplest Hamiltonians that can describe the quantum spin Hall (QSH) effect and edge states at the interface between inverted band HgTe quantum wells and normal insulators.

1.2 Topological insulator quantum dots

Semiconductor quantum dots (QDs) have also attracted a substantial amount of attention in the condensed matter physics community recently [29–39], driven by their potential applications as lasers, transistors, and single and entangled photon sources as building blocks in quantum technologies [33–39]. By the same token, interest in TI QDs has also gained traction [2, 3, 40–46].

Edge states arise naturally in the study of QDs in two-dimensional (2D) materials such as graphene [32]. Indeed, in normal semiconductors, edge states, being detrimental to the performance of the devices, are commonly passivated. This improves the performance of the device. By contrast, edge states in the non-trivial (inverted band) phase of the TI are robust and give rise to novel physics. For exam-

ple, one can envisage edge states in TIs as realizations of one-dimensional strongly interacting systems and, as will be discussed in section 3.2, sites in one-dimensional Hubbard models [47, 48].

The BHZ model has been used to study the edge states and the physical properties of HgTe TI QD structures. Chang et al. [40–42] and Zhu et al. [43] numerically analyzed helical edge states in cylindrical HgTe TI QDs. As well, Zhu et al. [44] studied the effects of tensile strain on rectangular QDs along the horizontal axis, concluding that irrespective of the deformations, edge states are robust and the energy gap increases. In addition to these works, Korkusinski and Hawrylak [3] studied HgTe TI disc QDs by using an eight-band three-dimensional (3D) $\vec{k}\cdot\vec{p}$ model, showing that edge states appear as a function of the thickness of the QD and applied strain. This work showed that by compressively straining HgTe TI QDs, one can control the quantized spin-Hall conductance in HgTe TIs which tunes the emergence and disappearance of edge states. This acts as the principle operation of quantum strain sensors based on strain-driven topological phase transitions in HgTe TI QDs.

Tight binding models [1, 5, 49–51] have also been used to understand the electronic and optical properties of TIs. Some of these tight-binding models [1, 51] have been used to investigate the edge states in HgTe QDs in TIs [51] and the optical absorption in HgTe quantum rings [49]. Such approaches are, however, numerical in nature and do not allow for a simple understanding of the physics of TI QDs.

In addition to these tight binding models [49,51], the optical properties of hybrid TI QD-nanoparticle systems [52] and nanomaterials [53, 54] have been studied to understand optical transitions and absorption of TIs. These works provide a theoretical perspective onto how light interacts with TIs.

This thesis contributes to the theory of the electronic and the optical properties

of quasi-2D QDs made of TIs described by a four-band BHZ model. The trivial versus topological properties of the bulk BHZ Hamiltonian are established by examining distinct topologies arising when mapping planes of wavevectors k_x, k_y onto Bloch spheres. It is shown that one set of material parameters defines the topologically non-trivial case, in which topologically protected edge states are found, and another set of parameters defines a topologically different map corresponding to a trivial insulator without edge states. We will explicitly relate the emergence of edge states to the material parameters and to the topology of the map, and characterize the transition from the topological to the normal regime.

In the topologically non-trivial case, nanostructures such as nanoribbons, quantum discs, and quantum squares support quantum states along the edges of the material. In the case of the nanoribbon, an analytical solution is found. From this and from numerical results of the quantum disc and square, the energy of the edge states, their decay length into the center of the QDs, and their position with respect to the physical edge is determined.

Moreover, it is shown that by straining the QDs, a topological phase transition occurs resulting in the disappearance of edge states. The Bir-Pikus Hamiltonian is introduced to account for strain. For the square quantum dot, edge states are studied as a function of compressive strain along both axes. It is found that by tuning the strain, the energy gap begins to close and when strain is tuned past a certain threshold, a topological phase transition occurs, leaving behind a trivial insulator vacant of edge states.

The optical response of the bulk BHZ system to circularly polarized light is also studied, yielding absorption coefficients with the strength dependent on the energy of the light. In particular, it is found that circularly polarized light is selectively

absorbed in TIs and couples with the spin of the TI.

1.3 Thesis outline

This thesis is organized as follows: in Chapter 1, we presented an introduction to the field of TIs and TI quantum dots. Chapter 2 describes the bulk properties of BHZ HgTe TIs. First, the BHZ Hamiltonian is derived by using $\vec{k} \cdot \vec{p}$ theory, then the quantum spin Hall effect in TIs is discussed. Afterwards, the topological phases of the BHZ model are examined by connecting the material parameters of the BHZ Hamiltonian to the topological phase transitions.

Chapter 3 presents part of the thesis' contribution to the field. It describes the application of the BHZ model to three different HgTe TI nanostructures: the nanoribbon, the quantum disc, and the quantum square. The methods used to diagonalize these quantum dot systems, and then the characteristics of their edge states, are explored. Chapter 4 presents the thesis' main contribution to the field. In there, the methods used to study the strain-induced topological phase transitions in HgTe TI quantum dots are discussed. Chapter 5 discusses the influence of light interacting with the quantum dots. Lastly, in Chapter 6, the conclusions and possible future directions of this work are mentioned.

Chapter 2

Bulk properties of mercury telluride topological insulators

In this chapter, we focus on the fundamental electronic properties of HgTe and the BHZ Hamiltonian. We begin by deriving the four-band BHZ Hamiltonian using the $\vec{k} \cdot \vec{p}$ method. We then discuss the QSH effect and the topological phases of the BHZ Hamiltonian. Finally, the topological phases are investigated by mapping the in-plane wavevectors through the BHZ Hamiltonian and onto a Bloch sphere. This allows us to understand the topological properties of TIs.

In the following section, 2.1, the $\vec{k} \cdot \vec{p}$ method is used to derive the BHZ Hamiltonian. The $\vec{k} \cdot \vec{p}$ method is a standard method [55] used in calculating the electronic structure of semiconductors in the vicinity of high symmetry points in k-space, such as around the Γ-point. The method was first used by Kane [56] to calculate the energy bands of semiconductors. While tight-binding models and density functional theory are also common methods used in computing the electronic structure of semiconductors, they provide more of an atomistic viewpoint. In contrast, the $\vec{k} \cdot \vec{p}$ method is marcoscopic and continuous which allows us to capture the physics of semiconductors

simply. Thus, for these reasons, the $\vec{k} \cdot \vec{p}$ method is chosen here to study TIs.

2.1 Four-band $\vec{k} \cdot \vec{p}$ BHZ Hamiltonian

Let us now construct the BHZ Hamiltonian using the $\vec{k} \cdot \vec{p}$ method. To begin, consider a single electron in an infinite crystal lattice. The Hamiltonian of a single electron can be written as a combination of kinetic and potential energies:

$$\hat{H} = \frac{\hat{p}^2}{2m} + V(\vec{r}) \tag{2.1}$$

where $\hat{p} = -i\hbar\vec{\nabla}$ is the momentum operator, m is the electron's mass, and $V(\vec{r})$ is the potential energy.

Suppose the system is periodic, then

$$V(\vec{r}) = V(\vec{r} + R) \tag{2.2}$$

where R is the translation lattice vector. The eigenstates ψ_{nk} of the Hamiltonian, Eq. (2.1), satisfy Bloch's theorem [57], taking the form:

$$\psi_{nk}(\vec{r}) = e^{i\vec{k}\cdot\vec{r}} u_{nk}(\vec{r}) \tag{2.3}$$

where n is the band index, k is the wavevector, and $u_{nk}(\vec{r} + R) = u_{nk}(\vec{r})$.

The time-independent Schrödinger equation (TISE) with the Hamiltonian, Eq. (2.1), and the wavefunction, Eq. (2.3), takes the form:

$$\left[\frac{(-i\hbar\vec{\nabla})^2}{2m} + V(\vec{r})\right] e^{i\vec{k}\cdot\vec{r}} u_{nk}(\vec{r}) = E_{nk} e^{i\vec{k}\cdot\vec{r}} u_{nk}(\vec{r}). \tag{2.4}$$

This leads to

$$H_{k\cdot p}u_{nk}(\vec{r}) = E_{nk}u_{nk}(\vec{r}) \tag{2.5}$$

where

$$H_{k\cdot p} = \frac{\left(\vec{\hat{p}}\right)^2}{2m} + V(\vec{r}) + \frac{\hbar^2\left(\vec{k}\right)^2}{2m} + \frac{\hbar\vec{k}\cdot\vec{p}}{m}. \tag{2.6}$$

Here, $H_{k\cdot p}$ is known as the $\vec{k}\cdot\vec{p}$ Hamiltonian.

Let us now recall that we are interested in the energy bands at the Γ-point in $\vec{k}\cdot\vec{p}$ theory, which in k-space is located at $k = 0$. We can expand u_{nk} in terms of a complete basis $u_{n,0}$ at the Γ-point:

$$u_{n,k}(\vec{r}) = \Sigma_m A_{m,k,n}u_{m,0}(\vec{r}) \tag{2.7}$$

where $A_{m,k,n}$ are some expansion coefficients.

HgTe is a heavy compound with such a strong spin-orbit coupling that it causes the p-band to be pushed above the s-band, creating a band inversion as shown in Fig. 2.1. For the $\vec{k}\cdot\vec{p}$ model, we consider HgTe's s-orbitals (Γ_6) and p-orbitals (Γ_8) shown in Fig. 2.1. The p-band, Γ_8, is a linear combination of p-orbitals $(X+iY)$ [3,58]. Expanding the Bloch function, Eq. (2.7), for these orbitals for the spin-up and spin-down electrons gives the four-element basis:

$$\begin{aligned} u_{n,k}(\vec{r}) = A_{k,n,S,m_j=1/2}\,|S\uparrow\rangle + A_{k,n,m_j=3/2}\,|\frac{1}{\sqrt{2}}(X+iY)\uparrow\rangle + A_{k,n,S,m_j=-1/2}\,|S\downarrow\rangle \\ + A_{k,n,m_j=-3/2}\,|-\frac{1}{\sqrt{2}}(X-iY)\downarrow\rangle\,. \end{aligned} \tag{2.8}$$

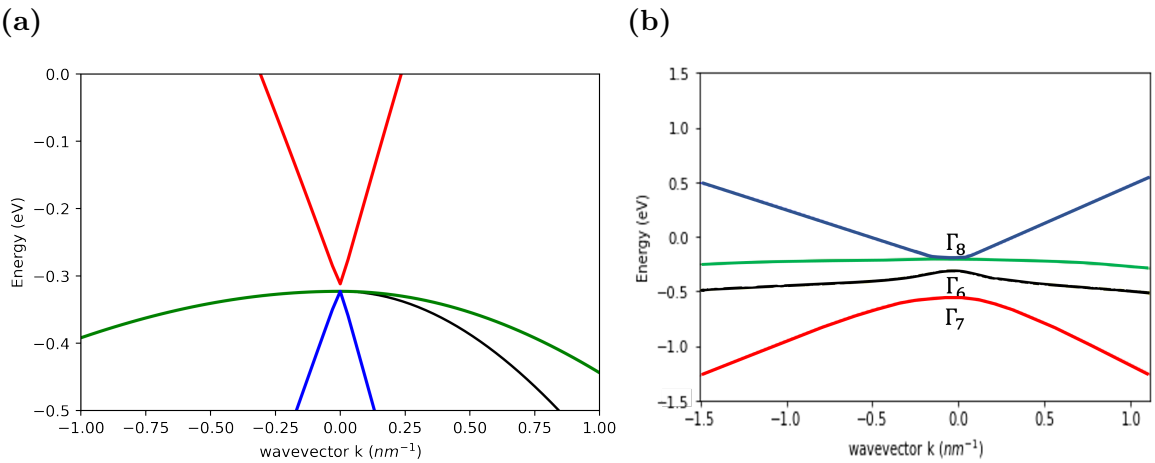

Figure 2.1: Bandstructure of HgTe around the Γ-point with (**a**) no spin-orbit coupling, we see the s-(black and red) and p-(blue and green) bands are not inverted, and in (**b**) when spin-orbit coupling is turned on, we see the p-(blue and green) bands have been pushed above the s-(black and red) bands creating a band inversion. In (**b**), the Γ_6 is the s-orbital band while Γ_8 and Γ_7 are the p-orbital bands split by spin-orbit coupling into a $J = 3/2$ band and $J = 1/2$ band, respectively [58]. Γ_6 is the conduction band and Γ_8 is the valence band in the BHZ model [58]. The figure is computed with *QNANO* [59], the parameters are found in A1 and is in agreement with previous well-known results [1, 58].

With the basis presented in Eq. (2.8), we can write a Hamiltonian matrix equation:

$$H = \begin{bmatrix} \langle S\uparrow|\, H_{k\cdot p}\,|S\uparrow\rangle & \langle S\uparrow|\, H_{k\cdot p}\,|\frac{1}{\sqrt{2}}(X+iY)\uparrow\rangle) & \langle S\uparrow|\, H_{k\cdot p}\,|S\downarrow\rangle & \langle S\uparrow|\, H_{k\cdot p}\,|\frac{1}{\sqrt{2}}(X-iY)\downarrow\rangle \\ \langle\frac{1}{\sqrt{2}}(X+iY)\uparrow|\, H_{k\cdot p}\,|S\uparrow\rangle & \langle\frac{1}{\sqrt{2}}(X+iY)\uparrow|\, H_{k\cdot p}\,|\frac{1}{\sqrt{2}}(X+iY)\uparrow\rangle & \langle\frac{1}{\sqrt{2}}(X+iY)\uparrow|\, H_{k\cdot p}\,|S\downarrow\rangle & \langle\frac{1}{\sqrt{2}}(X+iY)\uparrow|\, H_{k\cdot p}\,|\frac{1}{\sqrt{2}}(X-iY)\downarrow\rangle \\ \langle S\downarrow|\, H_{k\cdot p}\,|S\uparrow\rangle & \langle S\downarrow|\, H_{k\cdot p}\,|\frac{1}{\sqrt{2}}(X+iY)\uparrow\rangle & \langle S\downarrow|\, H_{k\cdot p}\,|S\downarrow\rangle & \langle S\downarrow|\, H_{k\cdot p}\,|\frac{1}{\sqrt{2}}(X-iY)\downarrow\rangle \\ \langle\frac{1}{\sqrt{2}}(X-iY)\downarrow|\, H_{k\cdot p}\,|S\uparrow\rangle & \langle\frac{1}{\sqrt{2}}(X-iY)\downarrow|\, H_{k\cdot p}\,|\frac{1}{\sqrt{2}}(X+iY)\uparrow\rangle & \langle\frac{1}{\sqrt{2}}(X-iY)\downarrow|\, H_{k\cdot p}\,|S\downarrow\rangle & \langle\frac{1}{\sqrt{2}}(X-iY)\downarrow|\, H_{k\cdot p}\,|\frac{1}{\sqrt{2}}(X-iY)\downarrow\rangle \end{bmatrix}. \tag{2.9}$$

In the case of HgTe, the nonzero spin-up matrix elements [5] in Eq. (2.9) are:

$$\langle S\uparrow|\, H_{k\cdot p}\,|S\uparrow\rangle = M + B(k_x^2 + k_y^2), \tag{2.10}$$

$$\langle\frac{1}{\sqrt{2}}(X+iY)\uparrow|\, H_{k\cdot p}\,|S\uparrow\rangle = v_f(k_x + ik_y), \tag{2.11}$$

$$\langle S\uparrow|\, H_{k\cdot p}\,|\frac{1}{\sqrt{2}}(X+iY)\uparrow\rangle = v_f(k_x - ik_y), \tag{2.12}$$

$$\langle\frac{1}{\sqrt{2}}(X+iY)\uparrow|\, H_{k\cdot p}\,|\frac{1}{\sqrt{2}}(X+iY)\uparrow\rangle = -M - B(k_x^2 + k_y^2) \tag{2.13}$$

where M is the energy gap parameter, B is proportional to the inverse of the effective mass, v_f is the Fermi velocity and we take $\hbar = 1$. The effective parameters M and B can be derived from a three-dimensional eight-band $\vec{k} \cdot \vec{p}$ theory for a given thickness of HgTe layer [3]. The spin-down matrix elements are found similarly.

Using the matrix elements, Eqs. (2.10)-(2.13), the effective four-band BHZ Hamiltonian is given by the following spin block diagonal:

$$H_{BHZ} = \begin{pmatrix} H_{\uparrow}(k) & 0 \\ 0 & H_{\downarrow}(k) \end{pmatrix}, \tag{2.14}$$

where

$$H_{\uparrow} = \begin{bmatrix} \frac{\Delta(k_x,k_y)}{2} & v_f(k_x - ik_y) \\ v_f(k_x + ik_y) & -\frac{\Delta(k_x,k_y)}{2} \end{bmatrix}. \tag{2.15}$$

Here, $\Delta(k_x, k_y) = 2(M + B(k_x^2 + k_y^2))$ is the decoupled conduction and valence band quasi-particle energy. The spin-down Hamiltonian in Eq. (2.14) is given by $H_{\downarrow}(k) = H_{\uparrow}^*(-k)$.

Now that we have derived the BHZ Hamiltonian, we will, in the next section, focus on the QSH effect and its theoretical prediction and experimental detection in HgTe/CdTe wells using the BHZ model. We will also touch on the link between the QSH effect and topological phases. This will prepare us for the discussion on the topological properties of the BHZ model in the last section of this chapter.

2.2 Quantum spin Hall effect in the BHZ model

In 1879, Edwin Hall carried out an experiment consisting of applying a magnetic field B perpendicular to a strip of metal, and then applying a current I along the $\hat{x}$-direction [60] as shown in Fig. 2.2. Hall observed that a positive charge moving

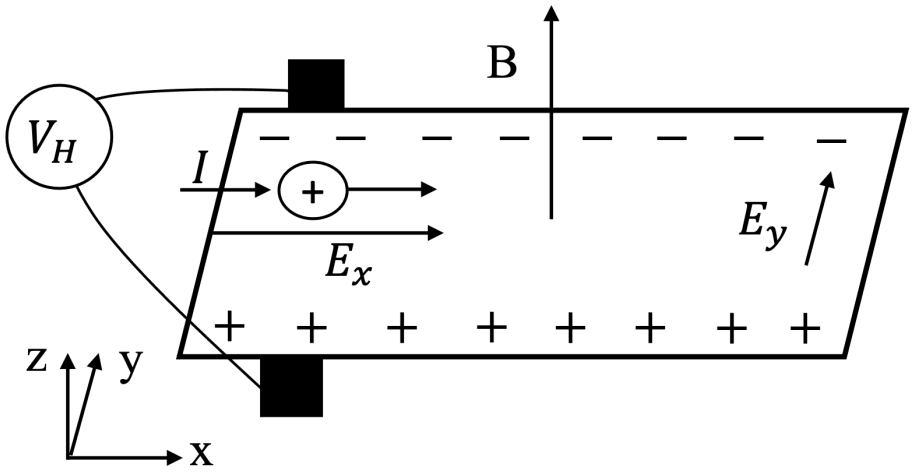

Figure 2.2: Schematic diagram of the Hall experiment. An electric field is seen along the $\hat{x}$-direction and a magnetic field is perpendicular to the surface, being applied in the $\hat{z}$-direction. The incoming positive charges are deflected to an edge of the sample by the Lorentz force, Eq (2.16), and a Hall voltage, V_H, can be measured across the sample.

with the current will, upon entering the magnetic field, be deflected to one of the edges of the material. This is due to the Lorentz force:

$$\vec{F} = q\left(\vec{E} + \vec{v} \times \vec{B}\right) \tag{2.16}$$

where $\vec{E}$ is the electric field, q is the electric charge, and $\vec{v}$ is the velocity of the charge.

Sometime later, as charges accumulate along the sample, an electric field in the $\hat{y}$-direction will be generated. In addition, a Hall resistance R_{xy} can be measured by Ohm's law:

$$R_{xy} = \frac{V_H}{I} \tag{2.17}$$

where V_H is the Hall voltage. Since V_H is generated in relation to the applied magnetic field, we expect a linear trend between B and R_{xy}.

However, von Klitzing et al. carried out experiments [61–63] on two-dimensional

electron gases at low temperatures and with high magnetic fields, observing that as B was tuned to higher values, V_H began to develop steps when B and R_{xy} were plotted against each other rather than the expected linear trend. Furthermore, these steps came in multiples of $R_{xy} = h/ne^2$ [64], where h is Planck's constant and n is an integer value with $n = 1, 2, 3, ...$ This phenomenon became known as the quantum Hall (QH) effect and is a topological phenomenon since this effect can be observed irrespective of the type of material [65]. This phenomenon was not observed in the Hall experiment since the experiment was performed at room temperature with weaker applied magnetic fields.

The QH effect does, however, breaks time-reversal symmetry (TRS) due to the presence of an external magnetic field [66]. Hence, the need to find materials that exhibit the QH effect without an applied magnetic field was highly sought-after. Haldane [67] was the first to propose the idea of quantum materials that can exhibit the QH effect without an external magnetic field. Building on Haldane's work, Kane et al. [68] predicted the quantum spin Hall (QSH) effect in graphene. Similarly, Zhang et al. [68–71] sought out to find a material where the QSH effect can be observed without breaking TRS in semiconductors. Shortly after Kane et al.'s proposal, Zhang et al. [5] theoretically predicted that if we consider certain special materials with strong spin-orbit (SO) interaction, then the spin will flow perpendicular to an applied electric field, as seen in Fig. 2.3. Hence, if a current flows through the sample, such as in Fig. 2.3, like the QH effect, the electrons will travel along "channels" at the edges of the materials. However, unlike the QH effect, this can happen without the presence of a magnetic field, the spins propagate in opposite directions, and is protected under TRS [71]. This is the QSH effect and it ensures immunity from impurities since the forward and backward propagation results from spin-momentum locking which locks

the spin perpendicular to the vector of the momentum [9, 71]. Indeed, if an electron encounters an impurity, it will simply travel in a path around it.

The distinguishing feature of Zhang et al.'s TI model from Haladane's [67] and Kane et al.'s work [68] is the presence of the energy gap in semiconducting materials, e.g., HgTe quantum wells. In addition to Zhang et al's [5] prediction, Molenkamp et

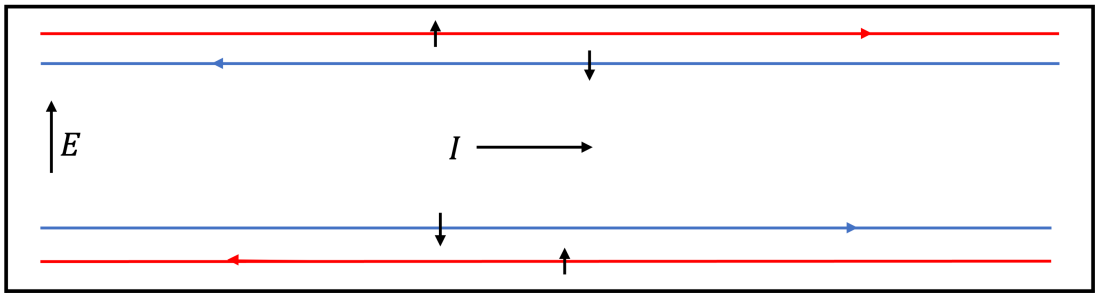

Figure 2.3: Schematic diagram showing the quantum spin Hall effect on a two-dimensional material. Along the edges, a spin current flows with spin-up and spin-down particles, and a spin-Hall conductance $G_{SH} = 2e^2/h$ can be measured [5].

al. [8] experimentally observed the QSH effect in HgTe quantum wells.

Now that we understand the QSH effect in semiconducting materials, let us discuss topology and how it is connected to TIs. The concept of topology arises in the study of geometric objects undergoing deformations. In such, objects can be classified geometrically by the number of holes present in them, e.g., a coffee cup with a handle has one hole and can be deformed into a donut which also has one hole; however, a sphere cannot be smoothly deformed into a donut since this would require creating a hole in the sphere. In the following section we will discuss and classify the topological properties of the HgTe TIs by studying the bulk properties of the BHZ Hamiltonian.

2.3 Topological properties of the BHZ model

A standard procedure in determining the topological properties of a Hamiltonian, is to take a map of wavevectors, (k_x, k_y) and map them through a normal of a vector containing the Hamiltonian parameters and onto a Bloch sphere [72]. In the BHZ model, two topologically different insulator phases can be realized. These two insulator phases are known as the trivial phase (normal bands) and non-trivial phase (inverted bands), and these phases can be seen by tuning M. This section presents a study of the transition of the BHZ Hamiltonian from a topological phase to a normal phase as a function of its parameters. This is done by mapping a plane of wavevectors (k_x, k_y) with the normal vector $\hat{n}(k_x, k_y) = \vec{d}(k_x, k_y)/|\vec{d}(k_x, k_y)|$ onto a Bloch sphere where $\vec{d}(k_x, k_y)$ is a vector of the material parameters of the BHZ Hamiltonian derived below.

To do this, let us first put the BHZ Hamiltonian matrix, Eq. (2.15), in a form that allows us to examine the global properties as a function of parameters in a convenient way. Decomposing Eq. (2.15) into three matrices, we get:

$$H_{\uparrow} = \frac{\Delta(k_x, k_y)}{2}\begin{bmatrix} 1 & 0 \\ 0 & -1 \end{bmatrix} + v_f k_x \begin{bmatrix} 0 & 1 \\ 1 & 0 \end{bmatrix} + v_f k_y \begin{bmatrix} 0 & -i \\ i & 0 \end{bmatrix}, \tag{2.18}$$

the Hamiltonian can thus take the form of the following compact Weyl-Hamiltonian:

$$H_{\uparrow} = \vec{d}\left(\vec{k}\right) \cdot \vec{\sigma}, \tag{2.19}$$

where pseudospin $\vec{\sigma}$ are the Pauli matrices, and the vector $\vec{d}(\vec{k})$ is given by

$$\vec{d}\left(\vec{k}\right) = \left(v_f k_x, v_f k_y, \frac{\Delta(k_x, k_y)}{2}\right). \tag{2.20}$$

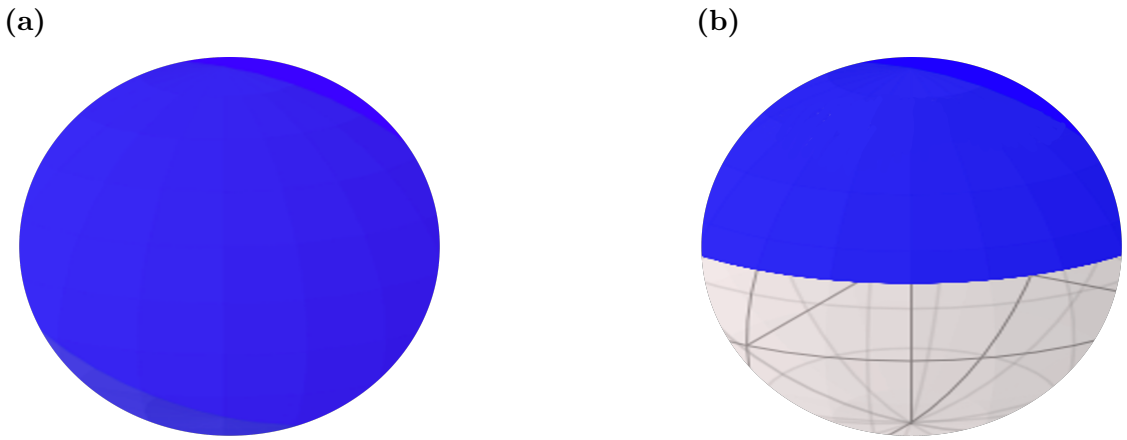

Figure 2.4: Mapping $\vec{n}$ of the (k_x, k_y) plane, values in the range $-10nm^{-1} < k_x < 10nm^{-1}$ and $-10nm^{-1} < k_y < 10nm^{-1}$, onto a Bloch sphere for the (**a**) topological, inverted band regime where $M < 0$ and $B > 0$, and (**b**) topologically trivial regime with normally ordered bands for $M > 0$ and $B > 0$. The topology of the two Bloch spheres is different; (**b**) contains a hole and (**a**) does not. The parameters of the topological non-trivial regime are $M = -150\text{meV}$, $B = 107\text{meV nm}^2$, and $v_f = 600\text{meVnm}$, while in the topologically trivial regime the parameters are $M = +150\text{meV}$, $B = 107\text{meVnm}^2$, and $v_f = 600\text{meVnm}$ [3].

We see that the bulk BHZ Hamiltonian, Eq. (2.19), is entirely specified by the vector $\vec{d}\left(\vec{k}\right)$. Let us attempt to understand the topology of the Hamiltonian. Define a normal vector $\hat{n}(k_x, k_y) = \vec{d}(k_x, k_y)/|\vec{d}(k_x, k_y)|$. This vector $\hat{n}$ can map the (k_x, k_y) plane onto the Bloch sphere.

Fig. 2.4a shows the values of $\hat{n}(k_x, k_y)$ mapped onto a Bloch sphere for $M < 0$ (inverted bands). In this case, the mapping converts the (k_x, k_y) plane onto the entire Bloch sphere. On the other hand, in Fig. 2.4b, the result of the mapping for $M > 0$ (normal bands) is shown, i.e., the sign of the energy gap is reversed. For this set of parameters, only the top part of the sphere is populated and there is a hole on the Bloch sphere. The hole can be understood as a fractional coverage of the Bloch sphere when mapped. Hence, we see that the topology of the Bloch sphere is different for the trivial ($M > 0$) and topological ($M < 0$) insulators. Thus, a trivial or topological insulator can be created by changing the sign of M and inverting the bands.

It will be shown in chapter 3, that the trivial insulator leads to normal energy bands with $|hh\rangle$ states contributing to the valence band, and $|e\rangle$ states contributing to the conduction band, while the non-trivial phase leads to a TI with inverted bands with $|e\rangle$ states contributing to the valence band, and $|hh\rangle$ states contributing to the conduction band and edge states existing inside the bulk energy gap. This will also be shown analytically in section 5.1 when analyzing the eigenvectors of the BHZ Hamiltonian, Eq. (2.15).

Now that we have established the possible topological phases a TI can exist in, and the consequences of such phases, we will proceed to studying quasi-2D HgTe TI's as QDs. In the following chapter, we will discuss the electronic properties of the edge states found in the non-trivial TI phase of nanoribbons, disc quantum dots, and square quantum dots. Proceeding this, we will discuss and show how we can transition between these topological phases by tuning the applied strain to the QD.

Chapter 3

Mercury telluride topological insulator quantum dots

Solids confined in all or most of their spatial dimensions are known as nanostructures [57]. 1D nanostrucures are confined in two spatial dimensions while 0D nanostructures are confined in all spatial dimensions. Examples of the former are nanoribbons and quantum wires whereas examples of the latter are semiconductors and nanoparticles [57]. A 0D nanostructure semiconductor where the electrons and holes are confined in all spatial dimensions are known as QDs. The confinement is usually produced electrostatically or via other material engineering [32, 73] and the QD size ranges from a few to hundreds of nanometers.

In such regard, an example of a quasi-2D QD TI is a finite lateral size quantum well of HgTe, embedded in a higher bandgap normal insulator material, such as CdTe [3,5]. In Chapter 2, we have discussed the effective quasi-2D BHZ $\vec{k} \cdot \vec{p}$ Hamiltonian. In this chapter, we use the BHZ Hamiltonian to study finite nanostructures of quasi-2D HgTe QDs: the square, the nanoribbon, and the disc as illustrated in Fig. 3.1. In these nanostructures, the wide bandgap insulator is replaced by a vacuum with an

infinite energy gap.

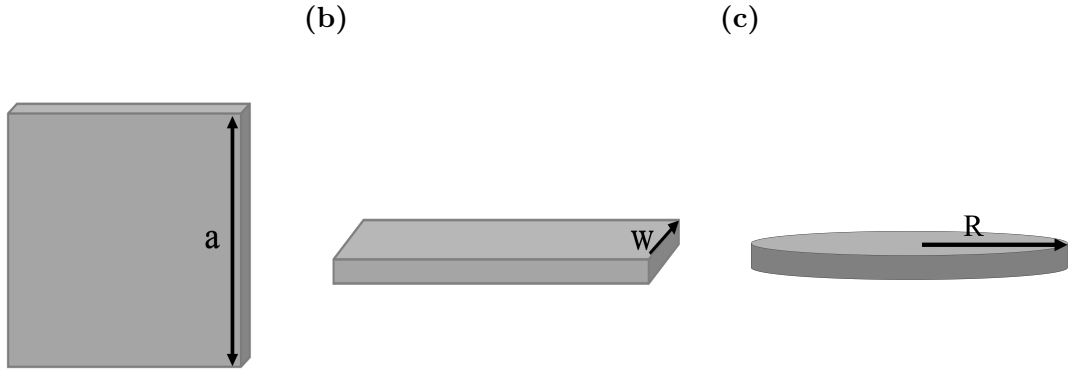

Figure 3.1: Schematic pictures of the geometries of quasi-2D HgTe TI nanostructures: (**a**) the square, (**b**) the nanoribbon, and (**c**) the disc.

3.1 Single particle states in HgTe TI nanostructures

In finite HgTe nanostructures, the motion of an electron is laterally confined by an external potential $V(x, y)$. The wavefunction $|\varphi_s \uparrow\rangle$ of the spin-up electron for such a nanostrucutre can be expressed as a linear combination of electron $|e \uparrow>$ and heavy hole $|hh \uparrow\rangle$ basis states, and envelope functions $f(x, y)$ and $g(x, y)$:

$$|\varphi_s \uparrow\rangle = A_s f(x, y) |e \uparrow\rangle + B_s g(x, y) |hh \uparrow\rangle . \tag{3.1}$$

These envelope functions, for a quantum dot level s, satisfy the time-independent Schrödinger Equation (TISE):

$$\begin{bmatrix} \frac{\Delta(\hat{p}_x,\hat{p}_y)}{2} + V(x, y) & v_f(\hat{p}_x - i\hat{p}_y) \\ v_f(\hat{p}_x + i\hat{p}_y) & -\frac{\Delta(\hat{p}_x,\hat{p}_y)}{2} - V(x, y) \end{bmatrix} \begin{bmatrix} A_s f(x, y) \\ B_s g(x, y) \end{bmatrix} = E_s \begin{bmatrix} A_s f(x, y) \\ B_s g(x, y) \end{bmatrix} \tag{3.2}$$

where $\hbar = 1$, and $\hat{p}_x = -i\partial/\partial x$ and $\hat{p}_y = -i\partial/\partial y$ are momentum operators acting on envelope functions *f(x,y)* and *g(x,y)*.

We proceed into the next sections by describing how we construct the wavefunctions and obtain the energy levels in HgTe TI nanostrucutures, beginning with the quantum square, then the nanoribbon, and lastly the quantum disc. This choice of order will allow us to gain a detailed intuitive sense of how one can construct a Hamiltonian matrix of a 2D TI QD, laying the foundation of how we study the quantum dots. However, to capture the electronic properties of these three geometries and draw similarities between them, we will discuss the energy spectra and edge states of the nanoribbon, followed by the quantum disc, and then the quantum square. Then we will build a connection between the 2D HgTe TI quantum disc described by the BHZ model and earlier works using $\vec{k} \cdot \vec{p}$ methods [3, 40]. This will establish validity in using the BHZ model and justify the discussion of edge states in the quantum square, allowing us to eventually move on to investigate the topological phases and the influence of strain on the edge states in TI QDs.

3.1.1 Energy levels and wavefunctions of HgTe TI quantum squares

We start our discussion of QDs with the HgTe TI square quantum dot, that is finite in the x- and y-directions with side length a as shown in Fig. 3.1a. We seek the wavefunction for an electron in a square quantum well given in terms of trigonometric functions $f_{n,m}(x, y)$, where n and m are integer quantum numbers. Our wavefunction takes a similar form to Eq. (3.1):

$$|\Psi^p(x,y)\rangle = \sum_{n,m} A^p_{n,m} f_{n,m}(x,y)\,|e\rangle + \sum_{k,l} B^p_{k,l} f_{k,l}(x,y)\,|hh\rangle \tag{3.3}$$

where $f_{n,m}(x,y) = \frac{2}{a} sin(\frac{n\pi x}{a}) sin(\frac{m\pi y}{a})$ and n and m are integer quantum numbers. The function $f_{n,m}(x,y)$ vanishes at the edges of the square.

Here the probability density of an electron localized at $\vec{r} = \vec{r_0}$ can be found by:

$$\langle \Psi^p(x,y)| \, \delta(\vec{r} - \vec{r_0}) \, |\Psi^p(x,y)\rangle = \sum_{n,m,q,r} \left(A^p_{n,m}\right)^\star A^p_{q,r} f_{n,m}(x_0,y_0) f_{q,r}(x_0,y_0) + \sum_{k,l,v,w} \left(B^p_{k,l}\right)^\star B^p_{v,w} f_{k,l}(x_0,y_0) f_{v,w}(x_0,y_0). \quad (3.4)$$

Similar to how Eq. (3.2) was constructed, we write out the TISE with the BHZ Hamiltonian, Eq. (2.14), and a spinor of the wavefunction, Eq. (3.3), which gives us the following eigenvalue problem:

$$\begin{bmatrix} M - B\left(\partial_x^2 + \partial_y^2\right) & v_f\left(-i\partial_x - \partial_y\right) \\ v_f(-i\partial_x + \partial_y) & -\left[M - B\left(\partial_x^2 + \partial_y^2\right)\right] \end{bmatrix} \begin{bmatrix} \sum_{n,m} A^p_{n,m} f_{n,m}(x,y) \\ \sum_{k,l} B^p_{k,l} f_{k,l}(x,y) \end{bmatrix} = E^p \begin{bmatrix} \sum_{n,m} A^p_{n,m} f_{n,m}(x,y) \\ \sum_{k,l} B^p_{k,l} f_{k,l}(x,y) \end{bmatrix}. \quad (3.5)$$

From Eq. (3.5) we arrive at the following two equations:

$$\left[M - B\left(\partial_x^2 + \partial_y^2\right)\right] \sum_{n,m} A^p_{n,m} f_{n,m}(x,y) + v_f\left(-i\partial_x - \partial_y\right) \sum_{k,l} B^p_{k,l} f_{k,l}(x,y) = E^p \sum_{n,m} A^p_{n,m} f_{n,m}(x,y), \quad (3.6)$$

$$v_f\left(-i\partial_x + \partial_y\right) \sum_{n,m} A^p_{n,m} f_{n,m}(x,y) - \left[M - B\left(\partial_x^2 + \partial_y^2\right)\right] \sum_{k,l} B^p_{k,l} f_{k,l}(x,y) = E^p \sum_{k,l} B^p_{k,l} f_{k,l}(x,y). \quad (3.7)$$

Suppose we project the eigenfunction $f_{q,r}(x,y)$ onto Eqs. (3.6) and (3.7), and integrate over all of space, then

$$\int_0^a dxdy[\sum_{n,m} A^p_{n,m}[M f_{q,r}(x,y)f_{n,m}(x,y) - B(f_{q,r}(x,y)\partial_x^2 f_{n,m}(x,y) + f_{q,r}(x,y)\partial_y^2 f_{n,m}(x,y)) + \sum_{k,l} B^p_{k,l}[v_f(-if_{q,r}(x,y)\partial_x f_{k,l}(x,y) - f_{q,r}(x,y)\partial_y f_{k,l}(x,y))] = E^p \sum_{n,m} A^p_{n,m} f_{q,r}(x,y)f_{n,m}(x,y)], \quad (3.8)$$

$$\int_0^a dxdy[\sum_{n,m} A^p_{n,m} v_f\,(-if_{q,r}(x,y)\partial_x f_{n,m}(x,y) + f_{q,r}(x,y)\partial_y f_{n,m}(x,y)) + \sum_{k,l} B^p_{k,l}[-M f_{q,r}(x,y)f_{k,l}(x,y) + B\left(f_{q,r}(x,y)\partial_x^2 f_{k,l}(x,y) + f_{q,r}\partial_y^2 f_{k,l}(x,y)\right)] = E^p \sum_{k,l} B^p_{k,l} f_{q,r}(x,y)f_{k,l}(x,y)]. \quad (3.9)$$

Also, it can be shown that

$$\frac{2}{a}\int_0^a dx\left[sin\left(\frac{q\pi x}{a}\right) sin\left(\frac{n\pi x}{a}\right)\right] = \delta_{q,n}. \quad (3.10)$$

Thus, using Eq. (3.10), Eqs. (3.8) and (3.9) become:

$$\left[M + B\left(\frac{q^2\pi^2}{a^2} + \frac{r^2\pi^2}{a^2}\right)\right] A^p_{q,r} + v_f \sum_{kl} \langle qr|\, V\, |kl\rangle\, B^p_{kl} = E^p A^p_{q,r}, \quad (3.11)$$

$$v_f \sum_{nm} \langle qr|\, V\, |nm\rangle\, A^p_{nm} + \left[-M - B\left(\frac{q^2\pi^2}{a^2} + \frac{r^2\pi^2}{a^2}\right)\right] B^p_{q,r} = E^p B^p_{q,r}, \quad (3.12)$$

where the coupling matrix elements are given by $\langle qr|\, V\, |kl\rangle = -i\delta_{r,l}\,\langle q|\,\partial_x\,|k\rangle -$

Table 3.1: HgTe square quantum dot matrix elements for the electronic states in s, p, and d shell

Matrix Element	Value
$\langle 1\vert\, \partial_x \,\vert 1\rangle$	0
$\langle 2\vert\, \partial_x \,\vert 1\rangle$	$8/3a$
$\langle 1\vert\, \partial_x \,\vert 2\rangle$	$-8/3a$
$\langle 2\vert\, \partial_x \,\vert 2\rangle$	0
$\langle 3\vert\, \partial_x \,\vert 1\rangle$	0
$\langle 1\vert\, \partial_x \,\vert 3\rangle$	0
$\langle 3\vert\, \partial_x \,\vert 2\rangle$	24/5a
$\langle 2\vert\, \partial_x \,\vert 3\rangle$	-24/5a

$\delta_{q,k} \langle r\vert\, \partial_y \,\vert l\rangle$, $\langle qr\vert\, V \,\vert nm\rangle = -i\delta_{r,m} \langle q\vert\, \partial_x \,\vert n\rangle + \delta_{q,n} \langle r\vert\, \partial_y \,\vert m\rangle$, and

$$\langle q\vert\, \partial_x \,\vert k\rangle = \frac{2}{a}\int_0^a sin\left(\frac{q\pi x}{a}\right) \partial_x sin\left(\frac{k\pi x}{a}\right) dx = \frac{2}{a}\frac{qk}{(k^2-q^2)}\left[(-1)^{q+k}-1\right] \quad (3.13)$$

if $q \neq k$, and if $q+k$ even then $\langle q\vert\, \partial_x \,\vert k\rangle = 0$; but if $q = k$ then integrand in Eq. (3.13) is odd, hence $\langle q\vert\, \partial_x \,\vert k\rangle = 0$.

Evaluating Eq. (3.13) for the quantum numbers q and k of the s, p, and d shells, we arrive at the results presented in Table 3.1. Hence, now that we have all of the ingredients to construct our Hamiltonian to be diagonalized, let us obtain, e.g., the energy spectrum for the s, p, and d shells of a HgTe TI square quantum dot of size $a = 28nm$.

To begin, define vectors of the quantum states for the s, p, and d shells: $|1,1\rangle$, $|1,2\rangle$, $|2,1\rangle$, $|2,2\rangle$, $|1,3\rangle$, and $|3,1\rangle$. Then, construct the $\langle qr\vert\, V \,\vert kl\rangle$ matrix in Eq. (3.11) for the pairs of states $|kl\rangle$ and $\langle qr|$. Afterwards, write out Eq. (3.11) for a given choice of $\langle qr|$. Below a example is shown for $\langle 1,1|$,

$$\left[M + 2B\frac{\pi^2}{a^2}\right] A^p_{1,1} + \langle 1,1\vert\, V \,\vert 1,1\rangle\, B^p_{1,1} + \langle 1,1\vert\, V \,\vert 1,2\rangle\, B^p_{1,2} + \langle 1,1\vert\, V \,\vert 2,1\rangle\, B^p_{2,1}$$

$$+ \langle 1,1|\, V\, |2,2\rangle\, B^p_{2,2} + \langle 1,1|\, V\, |1,3\rangle\, B^p_{1,3} + \langle 1,1|\, V\, |3,1\rangle\, B^p_{3,1} = E^p A^p_{1,1}, \quad (3.14)$$

where the coupling matrix elements can be found using the matrix elements , e.g., $\langle 1,1|\, \partial_x\, |1,1\rangle$ in Table 3.1 and is therefore $\langle 1,1|\, V\, |1,1\rangle = v_f\left(-i\,\langle 1|\, \partial_x\, |1\rangle - \langle 1|\, \partial_x\, |1\rangle\right) = 0$. Likewise, $\langle 1,1|\, V\, |1,2\rangle = v_f\left(-i\delta_{1,2}\,\langle 1|\, \partial_x\, |1\rangle - \delta_{1,1}\,\langle 1|\, \partial_x\, |2\rangle\right) = 8v_f/3a$. The other coupling matrix elements follow from this procedure.

A Hamiltonian matrix can be constructed by performing the aforementioned algorithm for each $|k,l\rangle$ and $\langle q,r|$ for the s, p, and d shells for both Eqs. (3.11) and (3.12) yielding:

$$\begin{bmatrix}
M+2B\frac{\pi^2}{a^2} & 0 & 0 & 0 & 0 & 0 & 0 & \frac{8v_f}{3a} & \frac{8v_f}{3a} & 0 & 0 & 0 \\
0 & M+5B\frac{\pi^2}{a^2} & 0 & 0 & 0 & 0 & \frac{-8v_f}{3a} & 0 & 0 & \frac{8iv_f}{3a} & \frac{24v_f}{5a} & 0 \\
0 & 0 & M+5B\frac{\pi^2}{a^2} & 0 & 0 & 0 & \frac{-i8v_f}{3a} & 0 & 0 & \frac{8v_f}{3a} & 0 & \frac{24iv_f}{5a} \\
0 & 0 & 0 & M+8B\frac{\pi^2}{a^2} & 0 & 0 & 0 & \frac{-8iv_f}{3a} & \frac{-8v_f}{3a} & 0 & 0 & 0 \\
0 & 0 & 0 & 0 & M+10B\frac{\pi^2}{a^2} & 0 & 0 & -\frac{24v_f}{5a} & 0 & 0 & 0 & 0 \\
0 & 0 & 0 & 0 & 0 & M+10B\frac{\pi^2}{a^2} & 0 & 0 & \frac{-24iv_f}{5a} & 0 & 0 & 0 \\
0 & \frac{-8v_f}{3a} & \frac{8v_f}{3a} & 0 & 0 & 0 & -M-2B\frac{\pi^2}{a^2} & 0 & 0 & 0 & 0 & 0 \\
\frac{8v_f}{3a} & 0 & 0 & \frac{8v_f i}{3a} & \frac{-24v_f}{5a} & 0 & 0 & -M-5B\frac{\pi^2}{a^2} & 0 & 0 & 0 & 0 \\
\frac{-8iv_f}{3a} & 0 & 0 & \frac{-8v_f}{3a} & 0 & \frac{24iv_f}{5a} & 0 & 0 & -M-5B\frac{\pi^2}{a^2} & 0 & 0 & 0 \\
0 & \frac{-8iv_f}{3a} & \frac{8v_f}{3a} & 0 & 0 & 0 & 0 & 0 & 0 & -M-8B\frac{\pi^2}{a^2} & 0 & 0 \\
0 & \frac{24v_f}{5a} & 0 & 0 & 0 & 0 & 0 & 0 & 0 & 0 & -M-10B\frac{\pi^2}{a^2} & 0 \\
0 & 0 & \frac{-24iv_f}{5a} & 0 & 0 & 0 & 0 & 0 & 0 & 0 & 0 & -M-10B\frac{\pi^2}{a^2}
\end{bmatrix}
\begin{bmatrix} A^p_{1,1} \\ A^p_{1,2} \\ A^p_{2,1} \\ A^p_{2,2} \\ A^p_{1,3} \\ A^p_{3,1} \\ B^p_{1,1} \\ B^p_{1,2} \\ B^p_{2,1} \\ B^p_{2,2} \\ B^p_{1,3} \\ B^p_{3,1} \end{bmatrix}
= E^p
\begin{bmatrix} A^p_{1,1} \\ A^p_{1,2} \\ A^p_{2,1} \\ A^p_{2,2} \\ A^p_{1,3} \\ A^p_{3,1} \\ B^p_{1,1} \\ B^p_{1,2} \\ B^p_{2,1} \\ B^p_{2,2} \\ B^p_{1,3} \\ B^p_{3,1} \end{bmatrix}. \quad (3.15)$$

The Hamiltonian in Eq. (3.15) was diagonalized using *NumPy*'s *linalg* package [74]. *linalg* is an open-source *Python* library that is dedicated to solving linear algebra problems. Specifically, the function *eigh*, of the *linalg* class is used to obtain the eigenvalues and eigenvectors of the Hamiltonian. *eigh* solves the eigenvalue problem using exact diagonalization from *LAPACK* routines. The spin-down Hamiltonian is diagonalized similarly.

Fig. 3.2b shows the eigenvalues for a square quantum dot of size $a = 28$nm using the vectors of quantum states of s, p, and d shells as the basis. While the basis used to produce Fig. 3.2b has not converged, the emergence of energy values in the inverted energy gap provides elementary verification of the methods employed here

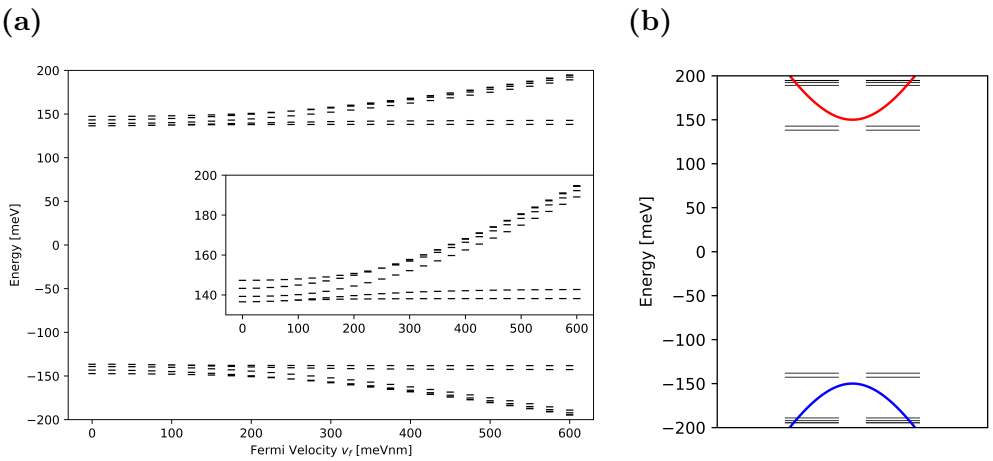

Figure 3.2: (**a**) Evolution of eigenvalues as a function of v_f for the spin-up Hamiltonian. Insert shows evolution of positive energy values. (**b**) Energy spectrum for the square HgTe TI quantum dot for $M = -150$meV, $B = 107$meV nm^2, and $v_f = 600$meVnm, for a basis consisting of s, p, and d shells. Black horizontal lines represent the eigenvalues found by numerical diagonalization of spin-up Hamiltonian Eq. (3.15) and spin-down similarly. Eigenvalues are plotted next to each other to show degeneracy. Red and blue curves represent the inverted energy bands as a function of momentum.

to study quantum dots. Moreover, even with such a small unconverged basis, we are able to study the influence of v_f on the eigenvalues. In Fig. 3.2a, as v_f is tuned, states are pushed out of the energy gap. Thus, v_f controls the coupling of basis states.

3.1.2 Energy levels and wavefunctions of HgTe TI nanoribbon

We continue our discussion of QDs with the HgTe nanoribbon; that is, a material infinite in the x-direction but finite in the y-direction with width W as shown in Fig. 3.1b. We seek the wavefunction for an electron in the nanoribbon in terms of plane waves with wavevector k_x in the x-direction and trigonometric functions $f_n(y)$

in the finite y-direction of the form:

$$|\Psi^p_{k_x}(x,y)\rangle = e^{ik_x x}\left[\sum_n A^p_{k_x,n} f_n(y)\,|e\rangle + \sum_m B^p_{k_x,m} f_m(y)\,|hh\rangle\right]. \tag{3.16}$$

The trigonometric functions $f_n(y)$ are eigenfunctions of a Hamiltonian of an electron in a quantum well of width W: $f_n(y) = \sqrt{\frac{2}{W}} sin(\frac{n\pi y}{W})$, where n is an integer quantum number. The functions $f_n(y)$ vanish at the edges of the nanoribbon.

We note that the probability of an electron localized at a position $y = y_0$ is given by:

$$\langle\Psi^p_{k_x}(y)|\,\delta(y-y_0)\,|\Psi^p_{k_x}(y)\rangle = \sum_{n,q}\left(A^p_{k_x,n}\right)^\star A^p_{k_x,q} f_n(y_0) f_q(y_0) + \sum_{m,r}\left(B^p_{k_x,m}\right)^\star B^p_{k_x,r} f_m(y_0) f_r(y_0). \tag{3.17}$$

The solution of Schrödinger's equation using the BHZ Hamiltonian in Eq. (2.15) and the wavefunction given in Eq. (3.16) requires that the eigenstates and eigenvalues for each k_x satisfy:

$$(M + Bk_x^2 + B\frac{n^2\pi^2}{W^2})A^p_{k_x,n} + v_f\sum_m (k_x\delta_{n,m} - \langle n|\,\partial_y\,|m\rangle)B^p_{k_x,m} = E^p_{k_x}A^p_{k_x,n}, \tag{3.18}$$

$$v_f\sum_m (k_x\delta_{n,m} + \langle n|\,\partial_y\,|m\rangle)A^p_{k_x,m} - (M + Bk_x^2 + B\frac{n^2\pi^2}{W^2})B^p_{k_x,n} = E^p_{k_x}B^p_{k_x,n} \tag{3.19}$$

where the matrix element $\langle n|\partial_y|m\rangle$ is given by Eq. (3.13). The eigenvectors $A^p_{k_x,n}$ and $B^p_{k_x,m}$, and eigenvalues $E^p_{k_x}$ are found by diagonalizing the Hamiltonian in Eqs. (3.18) and (3.19). The spin-down states can be obtained in a similar way. Next, we will discuss the procedure of calculating the energy levels and wavefunctions of an HgTe TI quantum disc.

3.1.3 Energy levels and wavefunctions of HgTe TI quantum discs

Following earlier work on 3D HgTe TI quantum discs [3, 40], we consider a circular quantum disc with radius R as shown in Fig. 3.1c, where the potential is infinite outside of the disc and zero inside. The wavefunction is a spinor characterized by pairs of angular momentum quantum numbers m in the conduction band and $m+1$ in the valence band for a state p. We expand the wavefunction in the basis of Bessel functions as:

$$|\Psi_m^p(r)\rangle = \sum_n A_n^{p,m}\phi_{n,m}(r)\,|e\rangle + \sum_s B_s^{p,m+1}\phi_{s,m+1}(r)\,|hh\rangle \tag{3.20}$$

where $\phi_{n,m}(r) = \frac{\sqrt{2}}{R}\frac{1}{|J_{m+1}(\alpha_m^n)|}J_m(\alpha_m^n\frac{r}{R})\frac{1}{\sqrt{2\pi}}e^{im\varphi}$, $J_m(\alpha_m^n\frac{r}{R})$ is the Bessel function of order m, and α_m^n is the n-th zero of the Bessel function of order m.

The probability of an electron localized at $r = r_0$ is given by:

$$\begin{aligned}\langle\Psi_m^p(r)|\,\delta(r-r_0)\,|\Psi_m^p(r)\rangle = &\sum_{n,q}\left(A_n^{p,m}\right)^\star A_q^{p,m}\phi_{n,m}(r_0)\phi_{q,m}(r_0)\\ &+\sum_{s,w}\left(B_s^{p,m+1}\right)^\star B_w^{p,m+1}\phi_{s,m+1}(r_0)\phi_{w,m+1}(r_0).\end{aligned} \tag{3.21}$$

The Hamiltonian, Eq. (2.15), in polar coordinates is given by

$$H_\uparrow = \begin{bmatrix}\frac{\Delta(\hat{k}_r)}{2} & v_f\hat{k}_-\\ v_f\hat{k}_+ & -\frac{\Delta(\hat{k}_r)}{2}\end{bmatrix}, \tag{3.22}$$

where $\frac{\Delta(\hat{k}_r)}{2} = M + B(-\frac{\partial^2}{\partial r^2} - \frac{1}{r}\frac{\partial}{\partial r} - \frac{1}{r^2}\frac{\partial^2}{\partial\varphi^2})$ is an intraband operator, and $\hat{k}_\mp = -ie^{i\varphi}(\frac{\partial}{\partial r}\mp i\frac{1}{r}\frac{\partial}{\partial\varphi})$ are operators connecting conduction and valence band states. Acting

with the Hamiltonian in Eq. (3.22) on the wavefunction given in Eq. (3.20), we arrive at the set of equations for amplitudes A and B:

$$\varepsilon_{n,m} A_n^{m,p} + iv_f \sum_s \langle m, n| \, k_- \, |m+1, s\rangle \, B_s^{m+1,p} = E^{m,p} A_n^{m,p}, \tag{3.23}$$

$$-iv_f \sum_s \langle m+1, n| \, k_+ \, |m, s\rangle \, A_s^{m,p} - \varepsilon_{n,m+1} B_n^{m+1,p} = E^{m,p} B_n^{m+1,p}, \tag{3.24}$$

where $\varepsilon_{n,m} = (M + B(\alpha_m^n)^2)$ and

$$\langle m, n| \, k_- \, |m+1, s\rangle = \left(\frac{2}{R} \frac{J_{m+1}(\alpha_m^n)}{|J_{m+1}(\alpha_m^n)|} \frac{J_{m+2}(\alpha_{m+1}^s)}{|J_{m+2}(\alpha_{m+1}^s)|} \frac{\alpha_m^n \alpha_{m+1}^s}{(\alpha_m^n)^2 - (\alpha_{m+1}^s)^2} \right), \tag{3.25}$$

$$\langle m+1, n| \, k_+ \, |m, s\rangle = \left(\frac{2}{R} \frac{J_{m+1}(\alpha_{m+1}^n)}{|J_{m+1}(\alpha_{m+1}^n)|} \frac{J_{m+2}(\alpha_m^s)}{|J_{m+2}(\alpha_m^s)|} \frac{\alpha_{m+1}^n \alpha_m^s}{(\alpha_{m+1}^n)^2 - (\alpha_m^s)^2} \right). \tag{3.26}$$

The eigenvectors $A_n^{m,p}$ and $B_s^{m+1,p}$, and eigenvalues $E^{m,p}$ are found by diagonalizing the Hamiltonian in Eqs. (3.23) and (3.24). The spin-down eigenvalues can be obtained analogously.

3.2 Edge states in HgTe topological insulator quantum dots

In this section, the electronic properties of the non-trivial phase of the nanoribbon, square, and disc HgTe TI QDs, obtained from numerical diagonalizations of their respective Hamiltonians discussed in section 3.1 are shown. The edge states are characterized by the decay length into the center of the quantum dots. By using the BHZ model, where the bandgap insulator is replaced by a vacuum with an infinite energy gap, we avoid uncertainties that would arise in the usual $\vec{k} \cdot \vec{p}$ treatment of materials with interfaces [75, 76]. Such uncertainties are due to the rapid varying potentials

at the interfaces in semiconducting materials, such as a quantum dot embedded in a non-vacuum material. This also implies that the quantum dots are treated as quantum wells in which the wavefunction of the electron is zero at the physical edge of the nanostructure. Hence, there is a need to find the position of the edge states away from the boundaries in HgTe TI quantum wells. This is done in this chapter by deriving an analytical solution of an edge state in the BHZ nanoribbon.

3.2.1 Edge states in an HgTe TI nanoribbon

We will now illustrate the electronic properties of nanoribbons by studying a nanoribbon with width $W=$ 100nm in the non-trivial, inverted band regime, i.e. $M < 0$. The energy levels $E^p_{k_x}$ obtained through the diagonalization of the Hamiltonian in Eqs. (3.18) and (3.19) as a function of wavevector k_x and subband p are shown in Fig. 3.3a. The energy levels inside the energy gap have a linear dispersion and there is an energy state with zero energy at $k_x = 0$ where the bands cross. As seen in Fig. 3.3b, these states are localized at the edges of the nanoribbon. The edge states in Fig. 3.3a are present until a threshold condition of k_x, namely $|k_x| < \sqrt{|M|/B}$, is met. At this threshold condition, the edge states become immersed in the bulk bands.

The electronic probability density of state $k_x = 0$ was obtained using Eq. (3.17), where the eigenvectors were found by numerically diagonalizing Eqs. (3.18) and (3.19). The probability density is plotted as a function of position y, shown in red in Fig. 3.3b, for the zero-energy edge state $k_x = 0$.

The numerically obtained edge state shown in Fig. 3.3b is a bonding superposition of two edge states localized on the left $y = 0$ and right $y = W$ edges of the nanoribbon. The electronic probability is zero at the physical edge $y = 0$, peaks at

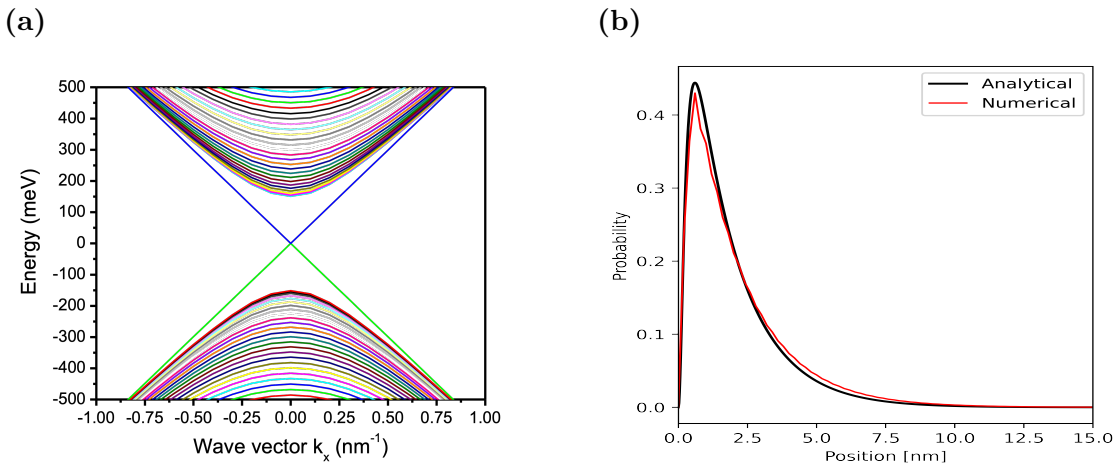

Figure 3.3: (**a**) Energy spectrum of the nanoribbon. We see states appearing in the bulk gap emerging from finite size quantization in the y-direction. (**b**) Total electronic probability as a function of position y for the electronic edge state at energy $E \sim 0$ at $k_x = 0$ in (**a**). Numerical results are in red, analytical results are in black. In both cases the edge state peaks at $y = 2$nm. The numerical electronic probability density function has two equal peaks at each edge of the quantum ribbon. We divide the analytical solution by a factor of 2 to compare with the numerical solution. Here, we are in the topological regime with parameters: $M = -150$meV, $B = 107$meVnm^2, and $v_f = 600$meVnm.

position $y = 2$nm and then decays into the bulk of the nanoribbon. Furthermore, the peak in the probability shows the position of the edge state away from the interface of the TI and vacuum.

Let us now derive the analytical solution for the zero-energy state in order to study the emergence of the edge state at this energy along with its position in space as a function of the material parameters, and to assess the accuracy of the numerical results.

Consider the energy spectrum of an HgTe nanoribbon shown in Fig. 3.3. In the energy gap, there are two eigenvalues at $E \sim 0$ and $k_x = 0$ corresponding to the linear combinations of wavefunctions localized on the left and right sides of the nanoribbon. For a wide nanoribbon, we can obtain a wavefunction localized at the edge $y = 0$ by

analyzing a semi-infinite plane. This state can be written as a combination of the electron and heavy hole states:

$$|\Psi_0\rangle = \sum_n A^0_{k_x,n} e^{ik_x x} g_n(y) |e\rangle + \sum_m B^0_{k_x,m} e^{ik_x x} g_m(y) |hh\rangle \tag{3.27}$$

evaluated at $k_x = 0$. In addition, at $k_x = 0$, the electron and heavy hole states share the same energy $E = 0$, hence their envelope functions $g(y)$ are identical. The wavefunction takes the form $|\Psi_0\rangle = Ag(y)|e\rangle + Ag(y)|hh\rangle$, where the function $g(y)$ is the eigenfunction of the Hamiltonian in Eq. (2.15) at zero energy $E = 0$ and with the wavevector $k_x = 0$, which satisfies the TISE:

$$\begin{bmatrix} M - B\partial_y^2 & -v_f\partial_y \\ v_f\partial_y & -[M - B\partial_y^2] \end{bmatrix} \begin{bmatrix} g(y) \\ g(y) \end{bmatrix} = 0. \tag{3.28}$$

The first equation in Eq. (3.28) can be written explicitly as

$$Mg(y) - B\partial_y^2 g(y) - v_f\partial_y g(y) = 0. \tag{3.29}$$

We choose a general solution of the form $g(y) = e^{-ky}$ that satisfies the differential equation. This solutions decays for large y if $ky > 0$. Substituting this form of $g(y)$ into Eq. (3.29) gives a characteristic equation for k:

$$-Bk^2 + v_f k + M = 0. \tag{3.30}$$

Eq. (3.30) has two solutions:

$$k_{1,2} = \frac{v_f \pm \sqrt{v_f^2 + 4BM}}{2B}. \tag{3.31}$$

We now analyze the two solutions: $M > 0$ corresponding to the trivial phase and $M < 0$ corresponding to non-trivial phase while keeping $B > 0$ and $v_f > 0$ in both cases.

In the trivial phase, $M > 0$, there are two solutions. The first solution, $k_1 \sim \frac{v_f}{B}$ is positive while the second solution, $k_2 = \frac{v_f - \sqrt{v_f^2 + 4BM}}{2B} < 0$, is negative and corresponds to the wavefunction exponentially growing for large y. Hence, in the trivial phase no edge states satisfying the boundary conditions can exist.

On the other hand, in the non-trival phase, $M < 0$, there are two solutions $k_{1,2} = \frac{v_f \pm \sqrt{v_f^2 - 4B|M|}}{2B}$. Close to $M = 0$, we find two positive real solutions: $k_1 \sim \frac{v_f}{B} > 0$ and $k_2 \sim 0$. These real positive solutions exist for gaps M satisfying $v_f^2 > 4B|M|$. With these two solutions we can construct an edge state at zero energy,

$$g(y) = N(e^{-k_1 y} - e^{-k_2 y}), \tag{3.32}$$

where this solution satisfies the boundary conditions $y = 0$ and $g(0) = 0$, and N is the normalization constant.

The maximum position of the edge state at zero energy can be found by taking the derivative of $g(y)$, Eq. (3.32), and setting it equal to zero, yielding the following solution:

$$y_{max} = \frac{1}{k_1 - k_2} ln \frac{k_1}{k_2}. \tag{3.33}$$

In Fig. 3.3b, in black, we show the probability density $|\Psi_0|^2/2$ as a function of the position away from the edge. Due to the analytical solution being restricted to a semi-infinite plane and since only one edge is considered, the entire probability density is in the region around the edge at $y = 0$ and decaying to zero for large y, as seen from the exponential decay in Eq. (3.32). Although, in the numerical case,

there is equal probability along both edges of the nanoribbon. Hence, to compare analytical to numerical results, Ψ_0 in the analytical solution is divided by 2. We see from this that the analytical formula predicts very well the position of the edge state and its decay into the material.

Hence, the appearance of edge states is directly related to the material parameters of the nanoribbon. Edge states appear only when M becomes negative and analogously, the topology of the Bloch sphere, Fig. 2.4a, changes. Thus, the material parameters influence the formation and the position of the electronic states localized at the edge and their decay into the bulk.

3.2.2 Edge states in an HgTe TI quantum disc

We now turn to the disc quantum dot. In this section, we aim to validate the BHZ model as a realistic model of TI QDs by comparing the results of quasi-2D BHZ QDs made of TIs with results obtain in the eight-band $\vec{k} \cdot \vec{p}$ disc model [3] and Chang et al.'s BHZ disc model [40]. In the quantum discs, the angular momentum $\hat{L}_z = m + \hat{s}_z$ is conserved where $\hat{s}_z = \pm 1/2$, the spins of the electron (spin-up or spin-down). For $\hat{s}_z = 1/2$, the energy spectrum is obtained via a numerical diagonalization of Eqs. (3.23) and (3.24) and likewise for numerical diagonalization of $H_\downarrow(k) = H_\uparrow^\star(-k)$. Results are depicted in Fig. 3.4a. Fig. 3.4a shows the energy levels of a disc with radius $R = 167$nm for parameters corresponding to the topological, inverted band regime with $M = -150$meV. We can see a discrete spectrum of valence and conduction band states. Additionally, inside the energy gap from -150meV to 150meV, we find a ladder of equally spaced edge states with linear dispersion as a function of angular momentum and energy bands. Moreover, here the quantum states at the edges of the disc are like finite edges of the HgTe TI nanoribbon with periodic boundary

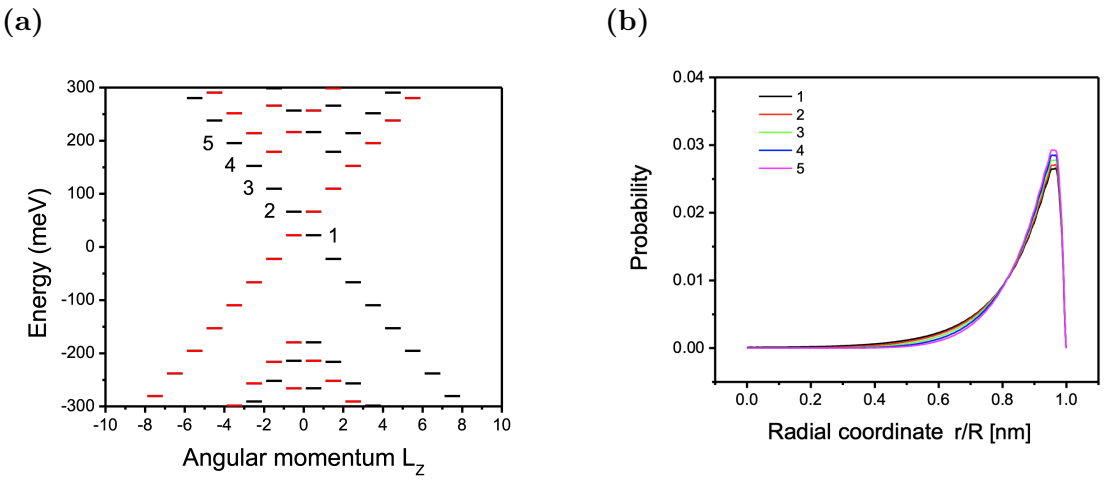

Figure 3.4: (**a**) Spectrum of energy levels for a disc TI QD as a function of total angular momentum $\hat{L}_z = m + \hat{s}_z$ for radius $R = 167$nm. Energy levels in the bulk gap are visible. Red levels correspond to the eigenvalues from spin-down and black levels to the eigenvalues from spin-up numerical diagoanlizations. (**b**) Electronic probability for states 1-5 shown in (**a**). The edge character of gap states and their position with respect to the edge are visible. The Hamiltonian in Eqs. (3.23) and (3.24) is numerically diagonalized with parameters $M = -150$meV, $B = 107$meVnm^2, and $v_f = 600$meVnm, corresponding to the topological regime.

conditions.

Fig. 3.4b shows the electronic probability density as a function of the radial coordinate for different edge states labeled in Fig. 3.4a. The electronic probability density is calculated using Eq. (3.21), by summing the eigenvectors for the angular momenta states in Fig. 3.4a. In Fig. 3.4b, we see that the electronic probability density peaks away from the physical edge and decays quickly into the center of the disc.

These results show that the electronic properties of the 2D four-band BHZ HgTe TI disc QD are in agreement with previous works on 3D eight-band HgTe TI disc QDs by Korkusinski et al. [3] and on BHZ results by Chang et al. [40]. This establishes validity in using the 2D BHZ model to describe HgTe TI QDs. Thus, we anticipate that the electronic properties and topological phase transitions found when

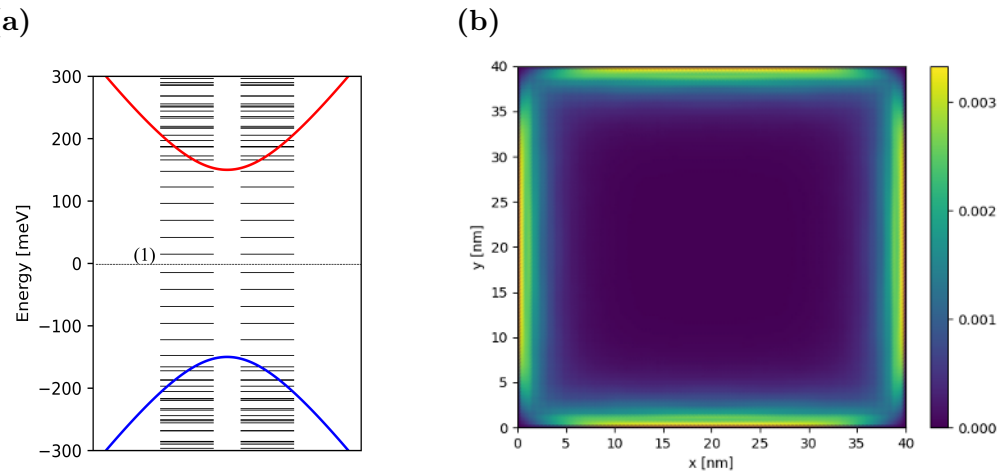

Figure 3.5: (**a**) Energy spectrum of the square quantum dot with lateral size $a =$ 40nm. Energy values are shown by the black horizontal lines. A ladder of equally spaced energy levels in the gap of the bulk material is visible. The Fermi level is at $E = 0$. The first energy level is labelled (1) and the spins are plotted next to each other to show degeneracy. Red and blue curves represent the inverted energy bands as a function of momentum. (**b**) Greyscale showing the probability of the first state above the Fermi level in (**a**). The parameters used in the diagonalization of the square quantum dot are the topological regime parameters: $M = -150$meV, $B = 107$meVnm^2, and $v_f = 600$meVnm.

compressively straining the 3D eight-band HgTe TI QDs will also be present when compressively straining the 2D four-band BHZ HgTe TI QDs.

3.2.3 Edge states in an HgTe TI quantum square

Let us discuss the last of the trio of HgTe TI QDs; the quantum square. The energy spectrum for a quantum square is obtained by diagonalizing Eqs. (3.11) and (3.12) for a basis of up to 24,200 states. The main difference between the quantum disc and the quantum square is the presence of sharp corners. As seen in Fig. 3.5b, the probability in these corners is approaching zero. Fig. 3.5a shows the energy spectrum of the square quantum dot with lateral size $a = 40$nm and inverted bands (red and blue curves) plotted using Eq. (5.3). We see a discrete spectrum of quantized energy levels in the conduction and valence bands while Fig. 3.5b shows the probability density

of the corresponding lowest energy conduction band state. In the energy window corresponding to a bulk energy gap, a ladder of equally spaced energy levels can be observed with the corresponding probability density, seen in Fig. 3.5b, being localized along the edges of the square and are expelled from the corners. The electronic probability density is obtained using Eq. (3.4).

Fig. 3.5b shows the formation of edge states with quantum barriers in the corners of the square. These edge states can be viewed as quantum rings [40], where electrons could be localized along the sides of the squares and can tunnel from edge-to-edge. These localized states would play the role of sites in the Hubbard model if they were populated with electrons, as these electrons would strongly interact if they were on the same site.

The emergence of edges states along the edges of the square QDs and the reproduction of results in previous works [3, 40] has established confidence in the 2D BHZ model as a realistic and accurate model to study quasi-2D HgTe TI QDs. Therefore, in the next chapter, we return to the notion of topological phase transitions with the objective of understanding emergence of edge states through studying topological phase transitions in a HgTe quantum square in a TI.

Chapter 4

Strain-driven topological phase transitions

In 1678, Robert Hooke [77] noticed that objects, such as springs, can be stressed and the resulting strain will be proportional to the applied stress; this can be measured by:

$$F = -kx \tag{4.1}$$

where F is the force exerted on the material, k is the spring constant, and x is the distance stretched from equilibrium.

In QDs, compressive strain could alter the electronic and optical properties of the nanostructure [3, 78]. Here, we study how compressive strain alters the electronic properties of HgTe TI square quantum dots as described by the BHZ model. Recall from chapter 2, the BHZ Hamiltonian can be derived using the $\vec{k} \cdot \vec{p}$ method. In the $\vec{k} \cdot \vec{p}$ method, the crystal is treated as a homogeneous continuous medium rather than a periodic array of atoms. Thus, in principle, one can view strain in the BHZ model similarly to how we view strain in a spring system.

4.1 Influence of strain in the BHZ model

To begin, let us specify the strain by the symmetric tensor [79]:

$$\varepsilon_{ij} = \frac{1}{2}\left(\frac{\partial u_i}{\partial x_j} + \frac{\partial u_j}{\partial x_i}\right), \tag{4.2}$$

where $u(x)$ is the displacement vector of a point in the solid due to the strain. Bir and Pikus [79] derived a Hamiltonian to account for the effects of strain, namely the four-band Bir-Pikus Hamiltonian, that is a simplified version of the eight-band Bir-Pikus Hamiltonian [3, 79], which is defined as:

$$H^{BP}_{\uparrow\downarrow}(k) = \begin{bmatrix} \hat{t} & 0 \\ 0 & \hat{u}+\hat{v} \end{bmatrix}, \tag{4.3}$$

where the operators $\hat{t} = a_c(\varepsilon_{xx} + \varepsilon_{yy})$, $\hat{u} = a_v(\varepsilon_{xx} + \varepsilon_{yy})$ and $\hat{v} = \frac{1}{2}b(\varepsilon_{xx} + \varepsilon_{yy})$ are written in terms of the strain tensor matrix elements ε_{ij}, Eq. (4.2), and a_c, a_v, and b are the deformation potentials. Note that we will utilize HgTe's deformation potential parameters found in van de Walle's work [80], $a_c = -4.60eV$, $a_v = -0.13eV$, and $b = -1.15eV$ in the calculations later in this chapter.

Following Korkusinski and Hawrylak's [3] approach, we add the spin-up Bir-Pikus Hamiltonian, Eq. (4.3), to the spin-up BHZ Hamiltonian, Eq. (2.15), resulting in the strain Hamiltonian:

$$H^{Strain}_{\uparrow}(k) = H^{BHZ}_{\uparrow}(k) + H^{BP}_{\uparrow}(k) = \begin{bmatrix} \frac{\Delta(k_x,k_y)}{2} - \hat{t} & v_f(k_x - ik_y) \\ v_f(k_x + ik_y) & -\frac{\Delta(k_x,k_y)}{2} + \hat{u} + \hat{v} \end{bmatrix}. \tag{4.4}$$

We also renormalize the gap to ensure that the Fermi level remains at $E = 0$. We

do this by taking a combination of energies at the bottom of the conduction band $E_c(k=0)$ and top of the valance band $E_v(k=0)$ at the Γ-point: $(E_c(k=0)+E_v(k=0))/2 = (\hat{t}+\hat{u}+\hat{v})/2$, and adding it to Eq. (4.4), arriving at:

$$H_{\uparrow}^{Strain}(k) = \begin{bmatrix} \frac{\Delta(k_x,k_y)}{2} - \frac{\gamma(\varepsilon)}{2} & v_f(k_x - ik_y) \\ v_f(k_x + ik_y) & -\frac{\Delta(k_x,k_y)}{2} + \frac{\gamma(\varepsilon)}{2} \end{bmatrix}, \tag{4.5}$$

where $\gamma(\varepsilon) = \hat{u} + \hat{v} - \hat{t}$ is the strain parameter and which describes the shift of the conduction and valance bands of the HgTe TI.

$\gamma(\varepsilon)$ acts as a tuning parameter, driving the TI square quantum dot from the non-trivial, topological phase to the trivial, normal phase. The strain tensors adjust the width and height of the square by $\varepsilon_{xx} = \Delta x/x$ and $\varepsilon_{yy} = \Delta y/y$.

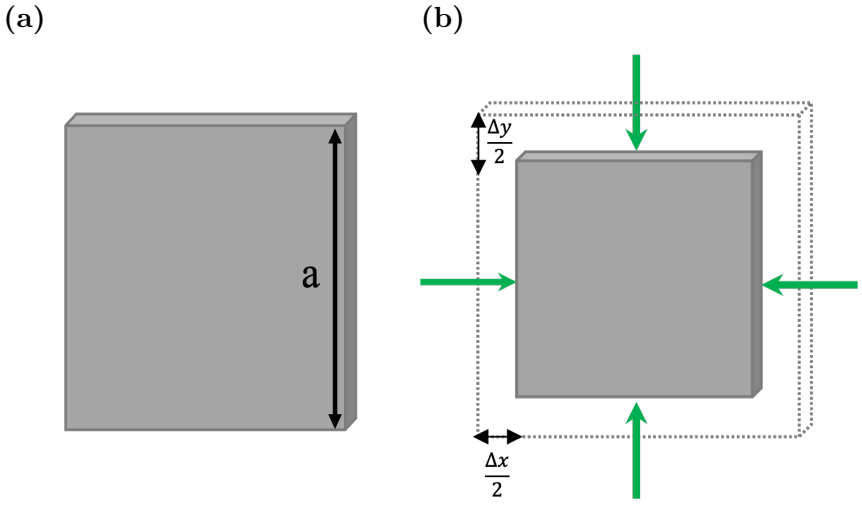

Figure 4.1: Schematic pictures of quasi-2D HgTe TI quantum dot systems. (**a**) Square quantum dot unstrained. (**b**) Square quantum dot after undergoing compressive stress in the horizontal and vertical directions resulting in the quantum dot reducing in size in both directions.

In this chapter, we consider the case when a square quantum dot is compressively strained in the horizontal and vertical directions as shown in Fig. 4.1. We then discuss the application of quantum dots as quantum strain sensors.

4.2 Tuning strain in HgTe square quantum dots: Topological phase transitions

Acting with the Hamiltonian, Eq. (4.5), on the wavefunction, Eq. (3.3), gives us a system of equations for the coefficients $A^p_{q,r}$ and $B^p_{q,r}$:

$$\left[M + B\left(\frac{q^2\pi^2}{a^2} + \frac{r^2\pi^2}{a^2}\right) - \frac{\gamma(\varepsilon)}{2}\right] A^p_{q,r} + v_f \sum_{kl} \langle qr| V |kl\rangle B^p_{kl} = E^p A^p_{q,r}, \tag{4.6}$$

$$v_f \sum_{nm} \langle qr| V |nm\rangle A^p_{nm} - \left[M + B\left(\frac{q^2\pi^2}{a^2} + \frac{r^2\pi^2}{a^2}\right) - \frac{\gamma(\varepsilon)}{2}\right] B^p_{q,r} = E^p B^p_{q,r}, \tag{4.7}$$

where the coupling matrix elements are given by $\langle qr| V |kl\rangle = -i\delta_{r,l} \langle q| \partial_x |k\rangle - \delta_{q,k} \langle r| \partial_y |l\rangle$ and $\langle qr| V |nm\rangle = -i\delta_{r,m} \langle q| \partial_x |n\rangle + \delta_{q,n} \langle r| \partial_y |m\rangle$ and $\langle q| \partial_x |k\rangle = \langle q| \partial_x |n\rangle$ is given by Eq. (3.13). The spin-up eigenvectors and eigenvalues can be found by diagonalizing Eqs. (4.6) and (4.7) while the spin-down eigenvectors and eigenvalues can be found similarly.

The emergence of edge states is related to strain by tuning $\gamma(\epsilon)$ until a topological phase transition occurs in square quantum dots. Fig. 4.2 shows that by progressively applying compressive stress in the horizontal and vertical directions of the square quantum dot, the dot becomes strained and an anti-inversion of bands occurs closing the inverted energy bands and opening normal energy bands. Then, as depicted in Figs. 4.2c and 4.2g at values of strain equal to $\varepsilon_{xx} = -0.0385$ and $\varepsilon_{yy} = -0.0385$, the energy bands form a Dirac cone and a topological phase transition occurs, hence these values act as the topological transition threshold. Upon applying compressive stress beyond this threshold, the bands become normally ordered and a gap of edge states opens. And in here, the quantum states are localized deep in the quantum dot, as depicted in Figs. 4.2d and 4.2h. Therefore, under sig-

nificant negative strain, the system is driven from the inverted band regime to the normal band regime. Thus, by this principle, the presence or absence of edge states can be detected in transport through the quantum dot. This can be experimentally realized if the dot is connected to a source and drain and current measurements are taken. This is also the principle physical operation of a quantum strain sensor [3] based on HgTe QDs in TIs.

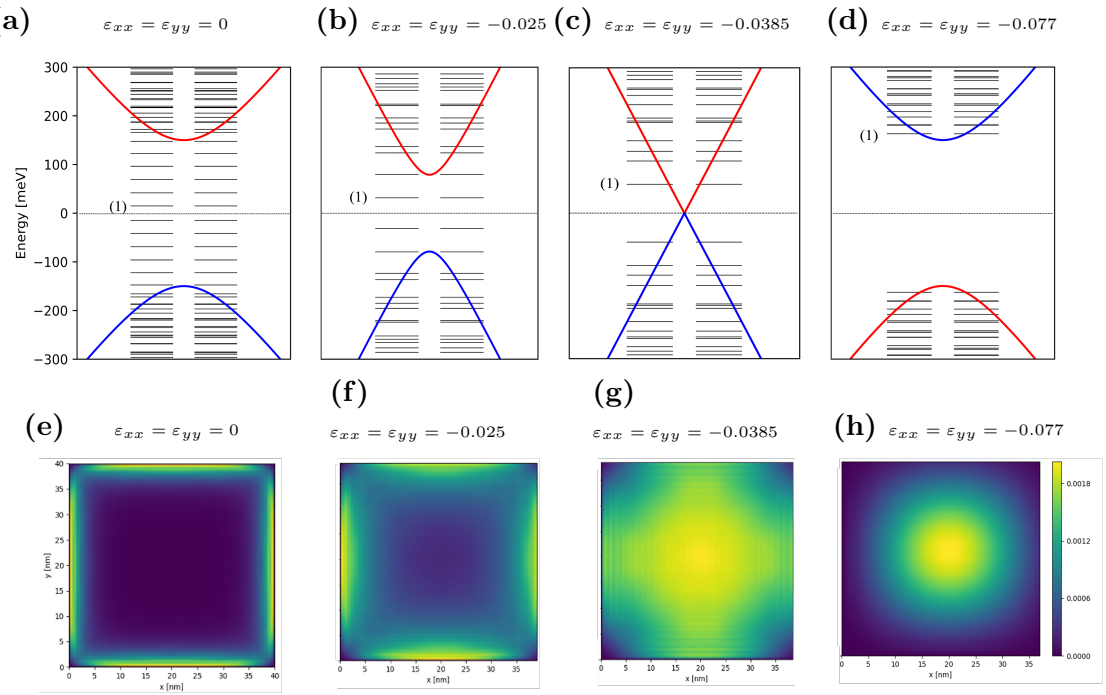

Figure 4.2: Energy spectra for four different cases of applied strain. (**a**) No strain applied, a topological insulator with a ladder of equally spaced energy levels in the gap of the bulk material is visible. The first energy level is labelled (1) and spin degeneracy are plotted. The black dotted line at zero energy denotes the Fermi level. (**b**) Some strain applied, the gap begins to close. (**c**) Dirac cone without edge states. (**d**) Normal insulator without states inside of the bulk gap. We see that by compressively straining the system, a topological phase transition occurs. (**e**)-(**h**) Greyscale showing the probability of the first state above the Fermi level in (**a**)-(**d**). The parameters used in the diagonalization of the square quantum dot are the topological regime parameters: $M = -150\text{meV}$, $B = 107\text{meVnm}^2$, and $v_f = 600\text{meVnm}$.

Chapter 5

Light matter interactions in mercury telluride topological insulators

The final chapter of this thesis is dedicated to a study of light interacting with HgTe TIs described by the BHZ model. To begin, the quantum theory of light was set in motion by Max Planck [81] in 1900. Planck measured the spectral distribution of the electromagnetic energy radiated by a thermal source, finding that the energy of a harmonic oscillator comes in quantized multiples of $\hbar\omega$, where ω is the frequency of light. Subsequently, in 1927, Paul Dirac, in his work on quantum electrodynamics [82], derived an expression to describe the transition rate from one quantum state to another. Enrico Fermi [83] generalized Dirac's work to describe the transition rate for any two-level system with a continuum of states that undergoes a weak perturbation. This method is known as Fermi's golden rule, and is a method used in studying the optical transition rates in two-level systems such as semiconductors and thus can be used to study how light interacts with HgTe TIs. In this chapter, we will use Fermi's

golden rule to derive the absorption coefficients of bulk HgTe TIs as a function of the energy of light $\hbar\omega$.

5.1 Absorption coefficients in bulk quasi-2D HgTe

Fermi's golden rule begins by considering a system in an initial eigenstate, say $|i\rangle$ of an unperturbed Hamiltonian H_0 and then considers the effects of a perturbation applied to the two-level system.

Let us begin by deriving the eigenvectors of the unperturbed BHZ Hamiltonian, Eq. (2.14), for both spins. First, we write Eq. (2.14) in polar coordinates:

$$H_{\uparrow,\downarrow}(k) = \begin{bmatrix} M + Bk^2 & v_f \tau k e^{-i\tau\theta} \\ v_f \tau k e^{i\tau\theta} & -(M + Bk^2) \end{bmatrix}, \tag{5.1}$$

where $\tau = \pm$ is the spin index, $+$ describes the spin-up Hamiltonian while $-$ describes the spin-down Hamiltonian. The Hamiltonian is written in polar coordinates using Euler's formula, i.e., $kcos(\theta) + iksin(\theta) = ke^{i\theta}$.

Acting with the BHZ Hamiltonian, Eq. (5.1), we will obtain eigenvalues and eigenvectors that satify the TISE:

$$\begin{bmatrix} M + Bk^2 & v_f \tau k e^{-i\tau\theta} \\ v_f \tau k e^{i\tau\theta} & -(M + Bk^2) \end{bmatrix} \begin{bmatrix} A_k^{\pm} \\ B_k^{\pm} \end{bmatrix} = E_{\pm}(k) \begin{bmatrix} A_k^{\pm} \\ B_k^{\pm} \end{bmatrix}. \tag{5.2}$$

The eigenvalues of Eq. (5.2), $E_{\pm}$ are found to be:

$$E_{\pm}(k) = \pm\sqrt{(M + Bk^2)^2 + (v_f k)^2}. \tag{5.3}$$

We can see from Eq. (5.3) that there are two eigenvalues, $E_+(k)$ and $E_-(k)$. Moreover,

when plotted, using HgTe parameters in the TI phase, we see that these eigenvalues are the inverted energy bands shown in Fig. 3.5a.

Recall that there are two phases of the normal, trivial ($M > 0$) and TI, non-trivial ($M < 0$). Consequently, this leads to two different eigenvalue problems to solve. The eigenvectors for the normal, trivial phase, using Eq. (5.2), can be found to be:

$$\Psi_k^{n,+} = \frac{1}{N_1}\begin{bmatrix} 1 \\ \tau\frac{\left(E_+^n(k)-\left(|M|+Bk^2\right)\right)}{v_f k}e^{i\tau\theta} \end{bmatrix}, \tag{5.4}$$

$$\Psi_k^{n,-} = \frac{1}{N_1}\begin{bmatrix} \tau\frac{\left(E_+^n(k)-\left(|M|+Bk^2\right)\right)}{v_f k}e^{i(-\tau\theta+\pi)} \\ 1 \end{bmatrix}, \tag{5.5}$$

and the eigenvectors for the TI, non-trivial phase can be found to be:

$$\Psi_k^{TI,+} = \frac{1}{N_2}\begin{bmatrix} \tau\frac{\left(E_+^{TI}(k)-\left(|M|-Bk^2\right)\right)}{v_f k}e^{-i\tau\theta} \\ 1 \end{bmatrix}, \tag{5.6}$$

$$\Psi_k^{TI,-} = \frac{1}{N_2}\begin{bmatrix} 1 \\ \tau\frac{\left(E_+^{TI}(k)-\left(|M|-Bk^2\right)\right)}{v_f k}e^{i(\tau\theta+\pi)} \end{bmatrix}, \tag{5.7}$$

where $N_1 = \sqrt{1+\frac{\left(E_+^n(k)-(|M|+Bk^2)\right)^2}{(v_f k)^2}}$ and $N_2 = \sqrt{1+\frac{\left(E_+^{TI}(k)-(|M|-Bk^2)\right)^2}{(v_f k)^2}}$ are the normalization factors, $E_+^n = \sqrt{(|M|+Bk^2)^2+(v_f k)^2}$, $E_+^{TI} = \sqrt{(|M|-Bk^2)^2+(v_f k)^2}$ and we have used the fact that $E_-^n(k) = -\sqrt{\left(|M|+Bk^2\right)^2+(v_f k)^2} = -E_+^n(k)$. $E_-^{TI}(k)$ can be found similarly.

To prove our claim in section 2.3 on the band inversion, and to gain a deeper intuitive sense of the bulk BHZ Hamiltonian, let us study the behaviour of the eigenvectors around the Γ-point of both phases of the BHZ model. To do this, we make use of the binomial approximation: $E_+^n(k) - (M+Bk^2) = \sqrt{(|M|+Bk^2)^2+(v_f k)^2} -$

$(M+Bk^2) = \frac{1}{2}\frac{(v_f k)^2}{M+Bk^2}$ with k being small. Thus, the eigenvectors for the trivial phase, Eqs. (5.4) and (5.5), around the Γ-point takes the form:

$$\Psi_k^{n,+} = \frac{1}{N_1}\begin{bmatrix} 1 \\ \tau\frac{1}{2}\frac{v_f k}{|M|+Bk^2}e^{i\tau\theta} \end{bmatrix}, \tag{5.8}$$

$$\Psi_k^{n,-} = \frac{1}{N_1}\begin{bmatrix} \tau\frac{1}{2}\frac{v_f k}{|M|+Bk^2}e^{i(-\tau\theta+\pi)} \\ 1 \end{bmatrix}, \tag{5.9}$$

and $N_1 = \sqrt{1+\frac{1}{4}\frac{(v_f k)^2}{(|M|+Bk^2)^2}}$. Similarly, the eigenvectors for non-trivial phase around the Γ-point will become:

$$\Psi_k^{TI,+} = \frac{1}{N_2}\begin{bmatrix} \tau\frac{1}{2}\frac{v_f k}{|M|-Bk^2}e^{-i\tau\theta} \\ 1 \end{bmatrix}, \tag{5.10}$$

$$\Psi_k^{TI,-} = \frac{1}{N_2}\begin{bmatrix} 1 \\ \tau\frac{1}{2}\frac{v_f k}{|M|-Bk^2}e^{i(\tau\theta+\pi)} \end{bmatrix}, \tag{5.11}$$

and $N_2 = \sqrt{1+\frac{1}{4}\frac{(v_f k)^2}{(|M|-Bk^2)^2}}$. We see that at the Γ-point, $k = 0$, the eigenvectors, Eqs. (5.8), (5.9), (5.10), and (5.11), become: $\Psi_{k=0}^{n,+} = (1,0) = |e>$, $\Psi_{k=0}^{n,-} = (0,1) = |hh>$, $\Psi_{k=0}^{TI,+} = (0,1) = |hh>$, and $\Psi_{k=0}^{TI,-} = (1,0) = |e>$. Hence, as seen in Fig. 5.1, the transition from the trivial to the non-trivial phase inverts the electron and heavy hole states. This analysis demonstrates an additional analytical proof that in the BHZ model, when undergoing a topological phase transition, the energy bands become inverted.

Now that we have derived the eigenvectors for each phase of the BHZ model, let us continue in calculating the absorption coefficient. We do this by first deriving

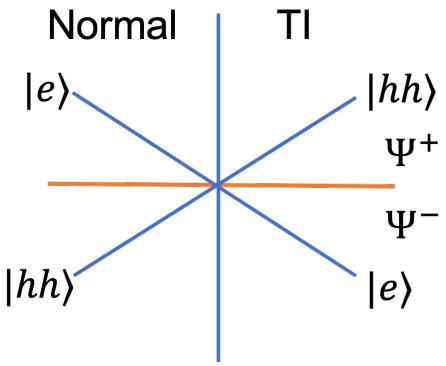

Figure 5.1: Evolution of electron and heavy hole states for the two phases of TIs at Γ-point. We see that in the normal, trivial phase, described by $M > 0$, the electronic states corresponding to the Ψ^+ eigenvector and the heavy hole state corresponds to the Ψ^- eigenvector at Γ-point. On the other hand, in the TI, non-trivial phase described by $M < 0$, the electronic states now correspond to Ψ^- eigenvector and the heavy hole states correspond to Ψ^+ eigenvector.

the Hamiltonian of the BHZ model when perturbed by circularly polarized light.

Consider circularly polarized light of the form:

$$\sigma^{\pm} : A_x^{\pm}(t) = \pm A_x^0 cos(\omega t), \tag{5.12}$$

$$A_y(t) = A_y^0 sin(\omega t), \tag{5.13}$$

where $\sigma^{\pm}$ denotes the polarization and ω is the frequency of light. We can find A_x^0 and A_y^0 using the Coulomb gauge: $\vec{E}(t) = -\frac{1}{c}\frac{d}{dt}\vec{A(t)}$, and we find them to be: $A_x^0 = cE_0/\omega$ and $A_y^0 = -cE_0/\omega$.

Fig. 5.2 shows the vector potentials as a function of ωt. Depending on the polarization chosen, the phase of light will change corresponding to two rotations: right-hand and left-hand circular polarization.

To obtain the perturbed Hamiltonian, we insert the vector potentials, Eq. (5.12) and Eq. (5.13), into the unpeturbed Hamiltonian, Eq. (5.1), written here in the, TI, non-trivial phase, using the momentum-wavevector relation $\vec{p} = \hbar\vec{k}$ and the gauge

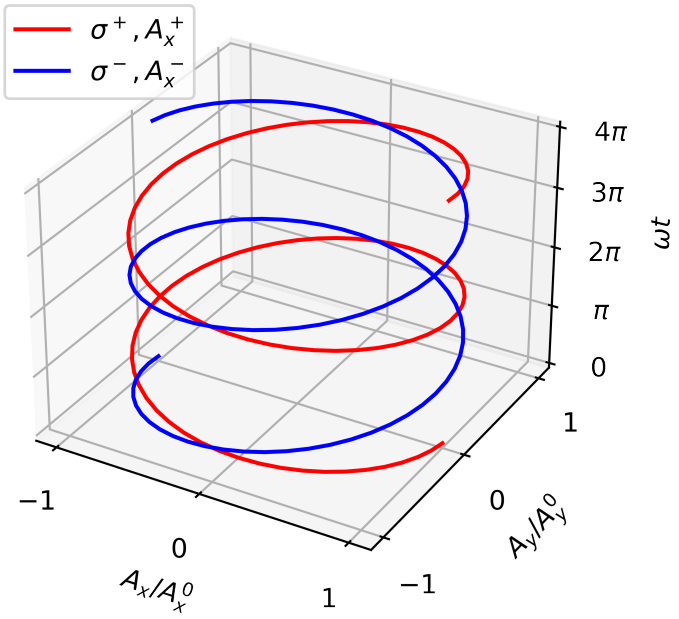

Figure 5.2: Vector potentials of circularly polarized light as a function of time. Here, the vector potentials propagate with different phases depending on the polarization.

transformation, $\vec{p} \to \vec{p} - \frac{e}{c}\vec{A}(t)$, and arrive at:

$$H_{\uparrow\downarrow} = \begin{bmatrix} -\left[|M| - \frac{B}{\hbar^2}\left(\left(p_x - \frac{e}{c}A_x^{\pm}(t)\right)^2 + \left(p_y - \frac{e}{c}A_y(t)\right)^2\right)\right] & \frac{v_f}{\hbar}\left(\tau p_x - \frac{\tau e}{c}A_x^{\pm}(t) - i(p_y - \frac{e}{c}A_y(t)\right) \\ \frac{v_f}{\hbar}\left(\tau p_x - \frac{\tau e}{c}A_x^{\pm}(t) + i\left(p_y - \frac{e}{c}A_y(t)\right)\right) & \left[|M| - \frac{B}{\hbar^2}\left(\left(p_x - \frac{e}{c}A_x^{\pm}(t)\right)^2 + \left(p_y - \frac{e}{c}A_y(t)\right)^2\right)\right] \end{bmatrix}. \tag{5.14}$$

Expanding Eq. (5.14) (for the spin-up case) and then ignoring the small $A^2(t)$ terms, we obtain:

$$H_{\uparrow} = \begin{bmatrix} -\left[|M| - \frac{B}{\hbar^2}\left(p_x^2 + p_y^2\right)\right] & \frac{v_f}{\hbar}\left(p_x - ip_y\right) \\ \frac{v_f}{\hbar}\left(p_x + ip_y\right) & \left[|M| - \frac{B}{\hbar^2}\left(p_x^2 + p_y^2\right)\right] \end{bmatrix} + g_1\vec{p}\cdot\vec{A}(t)\sigma_z$$
$$\mp g_2 g \begin{bmatrix} 0 & e^{\pm i\omega t} \\ e^{\mp i\omega t} & 0 \end{bmatrix} = H_{\uparrow}^{BHZ} + V(t), \tag{5.15}$$

where $g_1 = -2\frac{Be}{c\hbar^2}$, $g_2 = \frac{v_f e}{\hbar}$, and $g = \frac{E_0}{\omega}$. Thus, the interaction Hamiltonian takes

the form:

$$V(t) = g_1 \vec{p} \cdot \vec{A}(t)\sigma_z \mp g_2 g \begin{bmatrix} 0 & e^{\pm i\omega t} \\ e^{\mp i\omega t} & 0 \end{bmatrix}. \tag{5.16}$$

We now seek a time-dependent wavefunction in the basis of our unperturbed states:

$$\Psi(t) = C^+(t)e^{-\frac{i}{\hbar}E_+ t}\left|\Psi^+\right\rangle + C^-(t)e^{-\frac{i}{\hbar}E_- t}\left|\Psi^-\right\rangle, \tag{5.17}$$

where $|\Psi^\pm\rangle$ are eigenstates of the unperturbed BHZ Hamiltonian, Eqs. (5.4)-(5.7), with coefficients C^+ and C^- depending on time. To determine C^+ and C^-, we insert the wavefunction into the time-dependent Schrödinger equation (TDSE):

$$i\hbar\frac{\partial}{\partial t}\Psi(t) = \left(H_{BHZ} + V(t)\right)\Psi(t), \tag{5.18}$$

to obtain

$$\begin{aligned} i\hbar\frac{\partial C^+(t)}{\partial t}e^{-i\frac{E_+}{\hbar}t}\left|\Psi^+\right\rangle + i\hbar\frac{\partial C^-(t)}{\partial t}e^{-i\frac{E_-}{\hbar}t}\left|\Psi^-\right\rangle \\ = C^+(t)e^{-i\frac{E_+}{\hbar}t}V(t)\left|\Psi^+\right\rangle + C^-(t)e^{-i\frac{E_-}{\hbar}t}V(t)\left|\Psi^-\right\rangle. \end{aligned} \tag{5.19}$$

We then project $\langle\Psi^+|$ and $\langle\Psi^-|$ on Eq. (5.19), and utilize the orthogonality of $|\Psi^+\rangle$ and $|\Psi^-\rangle$ to obtain the following system of equations:

$$i\hbar\frac{\partial C^+(t)}{\partial t} = C^-(t)V_{+-}e^{i\frac{\Delta E}{\hbar}t} + C^+(t)V_{++}(t), \tag{5.20}$$

$$i\hbar\frac{\partial C^-(t)}{\partial t} = C^+(t)V_{-+}(t)e^{-i\frac{\Delta E}{\hbar}t} + C^-(t)V_{--}, \tag{5.21}$$

where $\Delta E = E^+ - E^-$ and

$$V_{++}(t) = \langle \Psi^+ | \, V(t) \, | \Psi^+ \rangle$$
$$= \frac{1}{N_2^2} \begin{bmatrix} f(k)e^{i\theta} & 1 \end{bmatrix} \left(g_1 \vec{p} \cdot \vec{A} \sigma_z \mp g g_2 \begin{bmatrix} 0 & e^{\pm i\omega t} \\ e^{\mp i\omega t} & 0 \end{bmatrix} \right) \begin{bmatrix} f(k)e^{-i\theta} \\ 1 \end{bmatrix}$$
$$= -\frac{g}{N_2^2} \left[g_1 \left(f^2(k) - 1 \right) \left(\pm k_x cos(\omega t) - k_y sin(\omega t) \right) \pm 2 g_2 f(k) cos(\theta \pm \omega t) \right]. \quad (5.22)$$

Here, $f(k) = (E_+^{TI} - (|M| - Bk^2))/v_f k$ or $f(k) = \frac{1}{2} \frac{v_f k}{|M| - Bk^2}$ around the Γ-point for k small. Additionally, we also redefine g_1 to be $g_1 = 2Be/\hbar$ in Eq. (5.22). From here, we also find that:

$$V_{+-}(t) = \langle \Psi^+ | \, V(t) \, | \Psi^- \rangle$$
$$= \mp \frac{g}{N^2} \left[2 g_1 k cos(\theta \pm \omega t) e^{i\theta} f(k) + g_2 (e^{\mp i\omega t} - e^{i(2\theta \pm \omega t)} f^2(k)) \right], \quad (5.23)$$

and

$$V_{--}(t) = \langle \Psi^- | \, V(t) \, | \Psi^- \rangle$$
$$= \frac{g}{N_2^2} \left[g_1 \left(f^2(k) - 1 \right) \left(\pm k_x cos(\omega t) - k_y sin(\omega t) \right) \pm 2 g_2 f(k) cos(\theta \pm \omega t) \right], \quad (5.24)$$

where once again g_1 is redefined as $g_1 = 2Be/\hbar$. Eqs. (5.22)-(5.24) are the matrix elements of the perturbation in the basis of unperturbed states.

Following methods by Faisal and Szulakowska [84,85], we put the unitary transformation of the basis:

$$C^+(t) = e^{-\frac{i}{\hbar} \int_0^t V_{++}(t') dt'} \tilde{C}^+(t), \quad (5.25)$$

$$C^-(t) = e^{-\frac{i}{\hbar} \int_0^t V_{--}(t') dt'} \tilde{C}^-(t), \quad (5.26)$$

into Eqs. (5.20) and (5.21), to obtain:

$$i\hbar\frac{\partial\tilde{C}^{+}(t)}{\partial_t} = e^{i\left(\frac{\Delta E}{\hbar}t-\int_0^t[V_{--}(t')-V_{++}(t')]dt'\right)}V_{+-}(t)\tilde{C}^{-}(t), \tag{5.27}$$

$$i\hbar\frac{\partial\tilde{C}^{-}(t)}{\partial_t} = e^{-i\left(\frac{\Delta E}{\hbar}t+\int_0^t[V_{--}(t')-V_{++}(t')]dt'\right)}V_{-+}(t)\tilde{C}^{+}(t). \tag{5.28}$$

We can see from Eqs. (5.22) and (5.24) that $V_{--}(t) = -V_{++}(t)$. Hence, Eqs. (5.27) and (5.28) become:

$$i\hbar\frac{\partial\tilde{C}^{+}(t)}{\partial_t} = e^{i\left(\frac{\Delta E}{\hbar}t\right)}e^{d(t)g}gV_{+-}(t)\tilde{C}^{-}(t), \tag{5.29}$$

$$i\hbar\frac{\partial\tilde{C}^{-}(t)}{\partial_t} = e^{-i\left(\frac{\Delta E}{\hbar}t\right)}e^{d(t)g}gV_{-+}(t)\tilde{C}^{+}(t), \tag{5.30}$$

where $d(t) = -i\int_0^t \left[2V'_{--}(t')\right]dt'$ and we have pulled out the g from V_{+-} and V_{-+}.

Expanding $\tilde{C}^{+}(t)$ and $\tilde{C}^{-}(t)$ in powers of g, while assuming g small, and then collecting powers of g, we arrive at:

$$\begin{aligned} i\hbar\tfrac{\partial}{\partial_t}\tilde{C}^{+,0}(t) &= 0, & i\hbar\tfrac{\partial}{\partial_t}\tilde{C}^{-,0}(t) &= 0, \\ i\hbar\tfrac{\partial}{\partial_t}g\tilde{C}^{+,1}(t) &= e^{i\frac{\Delta Et}{\hbar}}gV_{+-}(t)\tilde{C}^{-,0}(t), & i\hbar\tfrac{\partial}{\partial_t}g\tilde{C}^{-,1}(t) &= e^{-i\frac{\Delta Et}{\hbar}}gV_{+-}(t)\tilde{C}^{+,0}(t). \end{aligned} \tag{5.31}$$

We assume that since our system is a two-level system, $C^{-}(t=0) = 1$, thus from Eq. (5.31), we obtain

$$\tilde{C}^{+,1}(t) = \frac{\mp g}{N_2^2}[\left(g_1kf(k) - g_2f^2(k)\right)e^{2i\theta}\frac{\left(1-e^{\frac{i}{\hbar}(\Delta E\pm\hbar\omega)t}\right)}{(\Delta E\pm\hbar\omega)} + \left(g_1kf(k)+g_2\right)\frac{\left(1-e^{\frac{i}{\hbar}(\Delta E\mp\hbar\omega)t}\right)}{\Delta E\mp\hbar\omega}]. \tag{5.32}$$

Keeping resonant absorption terms $\omega - \Delta E/\hbar$ and ignoring $\omega + \Delta E/\hbar$ non-resonant

terms, we arrive at:

$$\sigma^+ : \tilde{C}^{+,1}(t) = \frac{-g}{N_2^2\nu}\left(g_1 k f(k) + g_2\right)\left(1 - e^{\frac{i\nu t}{\hbar}}\right), \tag{5.33}$$

$$\sigma^- : \tilde{C}^{+,1}(t) = \frac{g}{N_2^2\nu}\left(g_1 k f(k) - g_2 f^2(k)\right) e^{2i\theta}\left(1 - e^{\frac{i\nu t}{\hbar}}\right), \tag{5.34}$$

where $\nu = \Delta E - \hbar\omega$.

We now have all of the ingredients needed to obtain the transition rate γ_{fi}. Let us calculate it for the spin-up, σ^- polarization case. Expanding Eq. (5.33) we see that

$$\begin{aligned}\tilde{C}^{+,1}(t) &= \frac{g}{N_2^2\nu}\left(g_1 k f(k) - g_2 f^2(k)\right) e^{2i\theta}\left(1 - e^{\frac{i\nu t}{\hbar}}\right) \\ &= \frac{g}{N_2^2\nu}\frac{t/2}{t\hbar/2\hbar}\left(g_1 k f(k) - g_2 f^2(k)\right) e^{i\frac{\nu t}{2\hbar}+2i\theta}\left(e^{\frac{-i\nu t}{2\hbar}} - e^{\frac{i\nu t}{2\hbar}}\right) \\ &= -i\frac{g}{N_2^2\nu}\frac{t}{t\hbar/2\hbar}\left(g_1 k f(k) - g_2 f^2(k)\right) e^{i\frac{\nu t}{2\hbar}+2i\theta} sin\left(\frac{\nu t}{2\hbar}\right).\end{aligned} \tag{5.35}$$

Then $\gamma_{fi}^{-,\uparrow}$ becomes:

$$\begin{aligned}\gamma_{fi}^{-,\uparrow} = \frac{|\tilde{C}^{+,1}(t)|^2}{t} &= \frac{g^2 t^2}{t^3\hbar^2 N_2^4\left(\nu/2\hbar\right)^2}\left(g_1 k f(k) - g_2 f^2(k)\right)^2 sin^2\left(\frac{\nu t}{2\hbar}\right) \\ &= \frac{g^2}{\hbar N_2^4}\left(g_1 k f(k) - g_2 f^2(k)\right)^2 2\pi\delta(\nu),\end{aligned} \tag{5.36}$$

where $sin^2(\nu t/2\hbar)/(\nu/2\hbar)^2 \to t2\pi\hbar\delta(\nu)$ as $t \to \infty$. Eq. (5.36) is known as Fermi's Golden Rule.

Recall $\nu = \Delta E(k) - \hbar\omega$. Then from the delta function in Eq. 5.36, $\delta(\Delta E(k) - \hbar\omega))$, light will only make a transition if it has energy equal to the difference between the energies of conduction and valence bands. In particular, at the minima of the

inverted bands:

$$\hbar\omega = E_+(k=0) - E_-(k=0) = 300meV, \tag{5.37}$$

$$\rightarrow min(\hbar\omega) = 2|M|, \tag{5.38}$$

where $|M| = 150meV$.

For σ^+, we find:

$$\gamma_{fi}^{+,\uparrow} = \frac{g^2}{\hbar N_2^4}\left(g_1 k f(k) + g_2\right)^2 2\pi\delta(\nu). \tag{5.39}$$

Employing the aforementioned method, we find that the transition rate for the spin-down cases are related to the spin-up results by:

$$\gamma_{fi}^{+,\downarrow} = \gamma_{fi}^{-,\uparrow}, \tag{5.40}$$

$$\gamma_{fi}^{-,\downarrow} = \gamma_{fi}^{+,\uparrow}. \tag{5.41}$$

Let us inspire confidence in Eq. (5.39) by showing that in the limit when the diagonals of the BHZ Hamiltonian, Eq. (2.15), $M + Bk^2 = 0$ - the Hamiltonian of gapless graphene [32, 85] - by using the above-mentioned approach, we retrieve the well-known result of Fermi's Golden rule for gapless graphene.

Suppose we set $M + Bk^2 = 0$ in the BHZ Hamiltonian. Then in terms of the results of Eq. (5.36), this will lead to $f(k) = (\sqrt{(|M| - Bk^2)^2 + (v_f k)^2} - (|M| - Bk^2)) \rightarrow 0$ and $N_2^4 = 4$ and at the Γ-point, $k = 0$, yielding the result:

$$\gamma_{fi}^{+,\uparrow} = \frac{E_0^2 v_f^2 e^2}{\omega^2\hbar^3}\frac{\pi}{2}\delta(\nu). \tag{5.42}$$

Now that we have established confidence in our expressions for Fermi's golden

rule, let us calculate the absorption coefficient. We begin by calculating the probability of a photon of energy $\hbar\omega$ being absorbed by summing all of the transitions from filled states to empty states. Let us do this for the spin-up, σ^+ polarization:

$$P(\hbar\omega) = \Sigma_{k_x,k_y}\gamma_{fi}^{+,\uparrow}(\hbar\omega,k_x,k_y) = \Sigma_{k_x,k_y}\frac{g^2(\omega)}{N_2^4(k)\hbar}\left[g_1kf(k)+g_2\right]^2 2\pi\delta(\nu)$$
$$= \frac{1}{2\pi}\int\int dkkd\theta\frac{g^2}{N_2(k)^4\hbar}\left[g_1kf(k)+g_2\right]^2\delta(\nu) = g^2\frac{e^2}{\hbar^3}\int dE\frac{\partial k_E}{\partial E}k_E\zeta(k_E)\delta(\nu), \tag{5.43}$$

where $\zeta(k) = \left[g_1kf(k)+g_2\right]^2/N_2^4(k)$. Note that $\zeta(k_E) = \frac{\left[2Bk_Ef(k_E)+v_f\right]^2}{N_2^4(k_E)}$ where $k_E = \sqrt{\sqrt{\Omega^2 - 1/B^2(M^2-E^2)} - \Omega}$, and $\Omega = (v_f^2 - 2|M|B)/2B^2$ is found using Eq. (5.3). The radial dependence of Eq. (5.3) from Fig. 5.3 ensures that k is positive, and thus

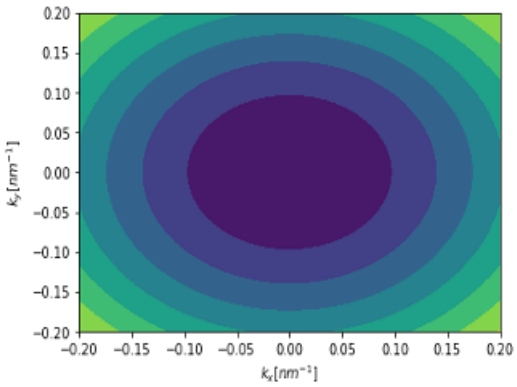

Figure 5.3: $E(k_x,k_y)$ plotted as a contour. We see that the energy has a radial dependence on $|\vec{k}|$, and concentric rings appear as $\vec{k}$ becomes larger.

we take the positive solutions of k_E. Lastly, note that
$(\frac{\partial k_E}{\partial E})k_E = E(k)/2\sqrt{B^4\Omega^2 - B^2(|M|^2-E^2)}$. Thus,

$$P(\hbar\omega) = g^2\frac{e^2}{\hbar^3}\frac{dk_E}{dE}k_E|_{E=\hbar\omega/2}\zeta(\hbar\omega/2)$$

$$= \frac{E_0^2 e^2}{4\omega\hbar^2} \frac{1}{\sqrt{B^4\Omega^2 - 4B^2\left(|M|^2 - \left(\frac{\hbar\omega}{2}\right)^2\right)}} \zeta\left(\frac{\hbar\omega}{2}\right). \quad (5.44)$$

The $E = \hbar\omega/2$ comes from the definition of ν: $\nu = \Delta E - \hbar\omega = 2E - \hbar\omega$ since $\Delta E = E_+ - E_- = 2E$ and $E_+ = -|E_-| = E$, and then using the sifting property of the δ-function.

We can now derive the absorption coefficient. To do this, consider the absorbed power W_a:

$$W_a = \hbar\omega P(\hbar\omega) = \frac{E_0^2 e^2}{4\hbar} \frac{1}{\sqrt{B^4\Omega^2 - 4B^2\left(|M|^2 - \left(\frac{\hbar\omega}{2}\right)^2\right)}} \zeta\left(\frac{\hbar\omega}{2}\right), \quad (5.45)$$

and the incident flux of light W_i is

$$W_i = \frac{c}{4\pi}|E|^2 = \frac{c}{4\pi}E_0^2. \quad (5.46)$$

The absorption coefficient A is:

$$A(\hbar\omega) = \frac{W_a}{W_i} = \pi\alpha \frac{1}{\sqrt{B^4\Omega^2 - 4B^2\left(|M|^2 - \left(\frac{\hbar\omega}{2}\right)^2\right)}} \zeta\left(\frac{\hbar\omega}{2}\right), \quad (5.47)$$

where $\alpha = e^2/\hbar c = 1/137$ is the fine structure constant. Using the minimum energy light must have to make a transition, Eq. (5.37), we find:

$$A^{+,\uparrow}(300meV) = \frac{2\pi\alpha}{1 - \frac{2|M|B}{v_f^2}} = 0.05, \quad (5.48)$$

with the parameters of HgTe in the TI phase taken here.

In Fig. 5.4a, we see that the the highest absorption occurs for energies slightly

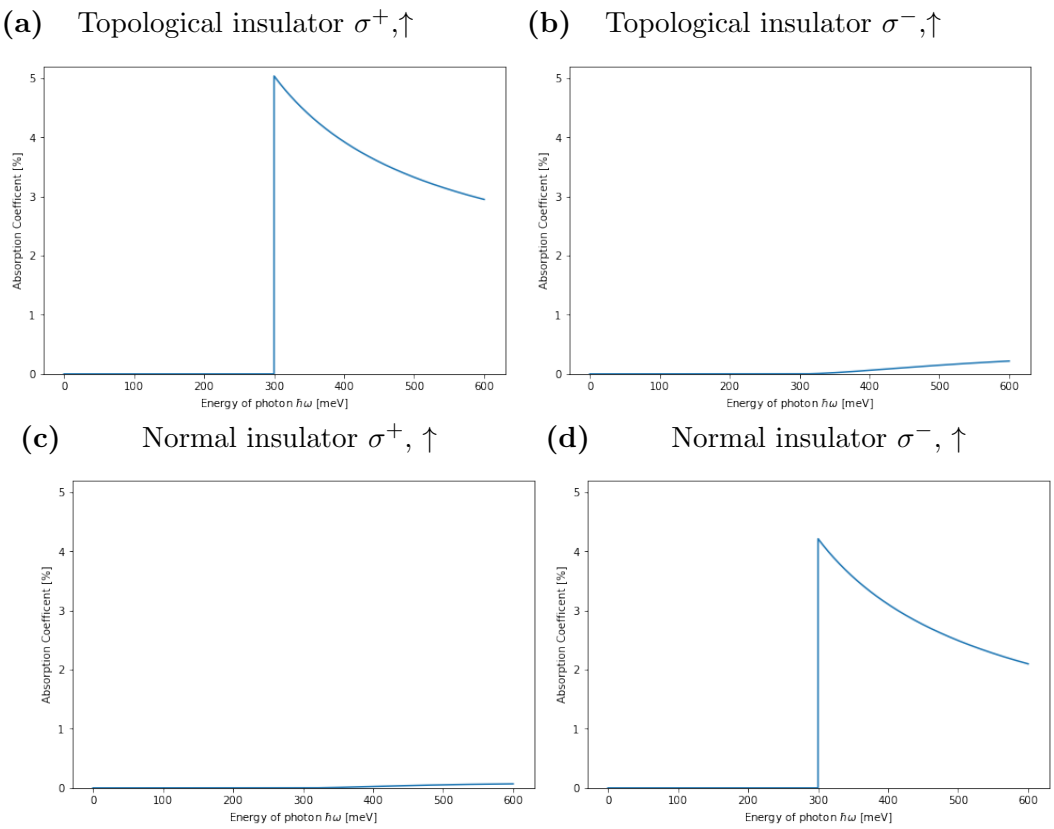

Figure 5.4: Absorption coefficients as a function of the frequency of light for: (**a**)-(**b**) the different polarizations, σ^+ and σ^-, of the non-trivial, TI phase. And for (**c**)-(**d**) the two different polarizations of the trivial, normal regime. We see that in both phases, the absorption is significantly higher in one polarization and then decays quickly as $\hbar\omega$ increases.

greater than the minimum energy required for light to make a transition, at around five percent, then decays as $\hbar\omega$ increases. This is as expected from the analysis in Eq. (5.48). Conversely, in Figs. 5.4b, the σ^- polarization, the absorption remains small for all energies of light. Likewise, when the system is in the trivial phase, we see low absorption in Fig. 5.4c and in Fig. 5.4d, we see a sharp peak very close to the minimum transition energy followed by a decay to zero as a function of energy.

In both the TI and normal insulator, light selectively couples to one spin polarization resulting in absorption peaks at the minimum energy required for light to

make a transition and is almost zero in the other polarization. Hence, one polarization is preferred in the absorption of circularly polarized light.

Proceeding, one may hypothesize that when considering quantum dots in TIs rather then bulk materials then the presence of edge states will play a role when calculating the absorption as the delta function will select energies between occupied edge states and empty edge states.

Chapter 6

Conclusions

This thesis contributed to the theory of the electronic and the optical properties of quasi two-dimensional nanostructures made of TIs. The HgTe TI quantum dots were described by the four-band BHZ Hamiltonian. The trivial versus topological properties of the BHZ Hamiltonian were inferred from the mapping of the 2D wavevector plane through the BHZ Hamiltonian onto a Bloch sphere. In the topologically nontrivial case, edge states were found in the nanoribbon, disc, and square geometries. The energy of the edge states, their decay length into the center of the quantum dot and, importantly, their position with respect to the physical edge, were determined.

It was shown that strain influences the electronic properties of TIs; particularly, the emergence and disappearance of edge states in TI QDs can be tuned as a function of applied compressive strain. In tuning the strain, the edge states began disappearing from the energy gap and after the quantum dot was significantly strained, a topological phase transition occurred, causing the TI to become a normal insulator without edge states. This allowed us to relate the emergence of edge states explicitly to the transition from the normal to the inverted band regime by the tuning of the applied strain to the square quantum dot. Nonetheless, in unstrained square QDs, edge

states were found to be localized along the sides of the square, with zero probability density in the corners. The existence of 1D edge states and quantum barriers in the corners may enable the design of quasi-one-dimensional quantum rings with localized electronic states along the edges, acting as tunable 1D Hubbard models. Conversely, in strained square quantum dots, the presence and absence of edge states and topological phase transitions can be controlled by tuning the applied strain, resulting in a modification of the electronic properties and the type of insulating phase. This principle can be used as a design model of a quantum strain sensor based on HgTe quantum dots in topological insulators via controlling the spin-Hall conductance.

The optical response of the bulk BHZ system to circularly polarized light was also studied, and the absorption coefficient was found to be dependent on the energy of the light. From this study, we conclude that circularly polarized light is selectively absorbed in and couples with the spin of the TI. Building on this may allow for a deeper understanding of the emergence of edge states based on the optical transitions in topological insulator quantum dots. Once the basic properties of light-matter interaction with TI QDs are understood deeper then one may progress further in the direction of studying the excitonic properties of HgTe QDs in TIs.

Topological insulators and topological materials in general have many fascinating novel applications [2, 3, 6, 9, 13, 14, 20–27, 45, 86–89]. They also offer a topological perspective of quantum physics. Exotic particles have also been predicted to exist in topological materials and topological insulators [65, 87, 88]. Therefore, studying topological materials and topological insulators further can perhaps improve our understanding of exotic particles through their connection to the standard model and topological field theory [65, 89], and this could, perhaps aid in our pursuit of unifying the laws governing the natural universe and the quantum world.

References

[1] G. Allan and C. Delerue, *Tight-binding calculations of the optical properties of hgte nanocrystals*, *Phys. Rev. B* **86** (Oct, 2012) 165437.

[2] B. Puzantian, Y. Saleem, M. Korkusinski, and P. Hawrylak, *Edge states and strain-driven topological phase transitions in quantum dots in topological insulators*, *Nanomaterials* **12** (2022), no. 23 4283.

[3] M. Korkusinski and P. Hawrylak, *Quantum strain sensor with a topological insulator hgte quantum dot*, *Scientific reports* **4** (2014), no. 1 1–6.

[4] M. F. L'Annunziata, *Radioactivity hall of fame-part i*, in *Radioactivity* (M. F. L'Annunziata, ed.), pp. 47–70. Elsevier Science B.V., Amsterdam, 2007.

[5] B. A. Bernevig, T. L. Hughes, and S.-C. Zhang, *Quantum spin hall effect and topological phase transition in hgte quantum wells*, *Science* **314** (Dec, 2006) 1757–1761.

[6] X.-L. Qi and S.-C. Zhang, *Topological insulators and superconductors*, *Rev. Mod. Phys.* **83** (Oct, 2011) 1057–1110.

[7] B. A. Volkov and O. A. Pankratov, *Two-dimensional massless electrons in an inverted contact*, *Pisma Zh. Eksp. Teor. Fiz.* **42** (1985) 145–148.

[8] M. Konig, S. Wiedmann, C. Brüne, A. Roth, H. Buhmann, L. W. Molenkamp, X.-L. Qi, and S.-C. Zhang, *Quantum spin hall insulator state in hgte quantum wells*, *Science* **318** (Nov, 2007) 766–770.

[9] D. Hsieh, Y. Xia, D. Qian, L. Wray, F. Meier, J. Osterwalder, L. Patthey, J. G. Checkelsky, N. Ong, A. V. Fedorov, et al., *A tunable topological insulator in the spin helical dirac transport regime*, *Nature* **460** (2009), no. 7259 1101–1105.

[10] M. Z. Hasan and C. L. Kane, *Colloquium: Topological insulators*, *Rev. Mod. Phys.* **82** (Nov, 2010) 3045–3067.

[11] Y. Ando, *Topological insulator materials*, *Journal of the Physical Society of Japan* **82** (Oct, 2013) 102001.

[12] B. A. Bernevig, *Topological insulators and topological superconductors*. Princeton university press, 2013.

[13] D. Kong, J. C. Randel, H. Peng, J. J. Cha, S. Meister, K. Lai, Y. Chen, Z.-X. Shen, H. C. Manoharan, and Y. Cui, *Topological insulator nanowires and nanoribbons*, *Nano letters* **10** (2010), no. 1 329–333.

[14] H. Peng, K. Lai, D. Kong, S. Meister, Y. Chen, X.-L. Qi, S.-C. Zhang, Z.-X. Shen, and Y. Cui, *Aharonov-bohm interference in topological insulator nanoribbons*, *Nature materials* **9** (2010), no. 3 225–229.

[15] C. Brüne, A. Roth, H. Buhmann, E. M. Hankiewicz, L. W. Molenkamp, J. Maciejko, X.-L. Qi, and S.-C. Zhang, *Spin polarization of the quantum spin hall edge states*, *Nature Physics* **8** (2012), no. 6 485–490.

[16] J. Maciejko, T. L. Hughes, and S.-C. Zhang, *The quantum spin hall effect*, *Annual Review of Condensed Matter Physics* **2** (2011), no. 1 31–53.

[17] A. Pertsova, C. M. Canali, and A. H. MacDonald, *Quantum hall edge states in topological insulator nanoribbons*, *Phys. Rev. B* **94** (Sep, 2016) 121409.

[18] P. Schüffelgen, D. Rosenbach, C. Li, T. W. Schmitt, M. Schleenvoigt, A. R. Jalil, S. Schmitt, J. Kölzer, M. Wang, B. Bennemann, et al., *Selective area growth and stencil lithography for in situ fabricated quantum devices*, *Nature nanotechnology* **14** (2019), no. 9 825–831.

[19] B. A. Levitan, L. Goutte, and T. Pereg-Barnea, *Surface theory of a second-order topological insulator beyond the dirac approximation*, *Phys. Rev. B* **104** (Sep, 2021) 125105.

[20] Y. Xia, D. Qian, D. Hsieh, L. Wray, A. Pal, H. Lin, A. Bansil, D. Grauer, Y. S. Hor, R. J. Cava, et al., *Observation of a large-gap topological-insulator class with a single dirac cone on the surface*, *Nature physics* **5** (2009), no. 6 398–402.

[21] Y. Chen, J. G. Analytis, J.-H. Chu, Z. Liu, S.-K. Mo, X.-L. Qi, H. Zhang, D. Lu, X. Dai, Z. Fang, et al., *Experimental realization of a three-dimensional topological insulator, bi2te3*, *science* **325** (2009), no. 5937 178–181.

[22] D. Hsieh, D. Qian, L. Wray, Y. Xia, Y. S. Hor, R. J. Cava, and M. Z. Hasan, *A topological dirac insulator in a quantum spin hall phase*, *Nature* **452** (2008), no. 7190 970–974.

[23] H. Zhang, C.-X. Liu, X.-L. Qi, X. Dai, Z. Fang, and S.-C. Zhang, *Topological insulators in bi2se3, bi2te3 and sb2te3 with a single dirac cone on the surface*, *Nature physics* **5** (2009), no. 6 438–442.

[24] E. Izquierdo, A. Robin, S. Keuleyan, E. L'huillier, and S. Ithurria, *Strongly confined hgte 2d nanoplatelets as narrow near-infrared emitters*, *Journal of the American Chemical Society* **138** (2016), no. 33 10496–10501.

[25] N. Moghaddam, C. Greboval, J. Qu, A. Chu, P. Rastogi, C. Livache, A. Khalili, X. Z. Xu, B. Baptiste, S. Klotz, et al., *The strong confinement regime in hgte two-dimensional nanoplatelets*, *The Journal of Physical Chemistry C* **124** (2020), no. 42 23460–23468.

[26] S. Keuleyan, E. Lhuillier, and P. Guyot-Sionnest, *Synthesis of colloidal hgte quantum dots for narrow mid-ir emission and detection*, *Journal of the American Chemical Society* **133** (2011), no. 41 16422–16424.

[27] S. Keuleyan, E. Lhuillier, V. Brajuskovic, and P. Guyot-Sionnest, *Mid-infrared hgte colloidal quantum dot photodetectors*, *Nature Photonics* **5** (2011), no. 8 489–493.

[28] L. Fu and C. L. Kane, *Topological insulators with inversion symmetry*, *Phys. Rev. B* **76** (Jul, 2007) 045302.

[29] L. Jacak, P. Hawrylak, and A. Wojs, *Quantum Dots*. Springer Verlag, 1998.

[30] D. Bimberg, M. Grundmann, and N. N. Ledentsov, *Quantum Dot Heterostructures*. John Wiley & Sons, 1999.

[31] P. Hawrylak and M. Korkusiński, *Electronic properties of self-assembled quantum dots*. Springer, 2003.

[32] A. D. Güçlü, P. Potasz, M. Korkusinski, and P. Hawrylak, *Graphene Quantum Dots*. Springer Verlag, 2014.

[33] Y. Arakawa and H. Sakaki, *Multidimensional quantum well laser and temperature dependence of its threshold current*, *Applied Physics Letters* **40** (1982), no. 11 939–941.

[34] S. Fafard, K. Hinzer, S. Raymond, M. Dion, J. McCaffrey, Y. Feng, and S. Charbonneau, *Red-emitting semiconductor quantum dot lasers*, *Science* **274** (1996), no. 5291 1350–1353.

[35] M. Bayer, P. Hawrylak, K. Hinzer, S. Fafard, M. Korkusinski, Z. Wasilewski, O. Stern, and A. Forchel, *Coupling and entangling of quantum states in quantum dot molecules*, *Science* **291** (2001), no. 5503 451–453.

[36] M. Ciorga, A. S. Sachrajda, P. Hawrylak, C. Gould, P. Zawadzki, S. Jullian, Y. Feng, and Z. Wasilewski, *Addition spectrum of a lateral dot from coulomb and spin-blockade spectroscopy*, *Phys. Rev. B* **61** (Jun, 2000) R16315–R16318.

[37] O. Benson, C. Santori, M. Pelton, and Y. Yamamoto, *Regulated and entangled photons from a single quantum dot*, *Phys. Rev. Lett.* **84** (Mar, 2000) 2513–2516.

[38] I. Schwartz, D. Cogan, E. R. Schmidgall, Y. Don, L. Gantz, O. Kenneth, N. H. Lindner, and D. Gershoni, *Deterministic generation of a cluster state of entangled photons*, *Science* **354** (2016), no. 6311 434–437.

[39] P. Laferrière, E. Yeung, M. Korkusinski, P. J. Poole, R. L. Williams, D. Dalacu, J. Manalo, M. Cygorek, A. Altintas, and P. Hawrylak, *Systematic study of the emission spectra of nanowire quantum dots*, *Applied Physics Letters* **118** (2021), no. 16 161107.

[40] K. Chang and W.-K. Lou, *Helical quantum states in hgte quantum dots with inverted band structures*, *Phys. Rev. Lett.* **106** (May, 2011) 206802.

[41] J. Li, W.-K. Lou, D. Zhang, X.-J. Li, W. Yang, and K. Chang, *Single- and few-electron states in topological-insulator quantum dots*, *Phys. Rev. B* **90** (Sep, 2014) 115303.

[42] W.-K. Lou, W. Yang, and K. Chang, *Helical conducting edge states in narrow-gap semiconductors without band inversion*, *Phys. Rev. B* **105** (Jan, 2022) 045305.

[43] F. Liu, J. Li, and J.-J. Zhu, *The single and coupled BHZ quantum dots with spin-orbit interaction*, *Solid State Communications* **330** (2021) 114275.

[44] J. Li, S. Zhang, Jian, and J.-J. Zhu, *Electronic structure of rectangular hgte quantum dots*, *Phys. E* **93** (2017) 58–62.

[45] M. S. Rider, M. Sokolikova, S. M. Hanham, M. Navarro-Cía, P. D. Haynes, D. K. Lee, M. Daniele, M. C. Guidi, C. Mattevi, S. Lupi, et al., *Experimental signature of a topological quantum dot*, *Nanoscale* **12** (2020), no. 44 22817–22825.

[46] M. S. Rider and V. Giannini, *Proposal for thz lasing from a topological quantum dot*, *Nanophotonics* **10** (2021), no. 13 3497–3506.

[47] I. Ozfidan, A. H. Trojnar, M. Korkusinski, and P. Hawrylak, *Geometry, chirality, topology and electron–electron interactions in the quadruple quantum dot molecule*, *Solid state communications* **172** (2013) 15–19.

[48] I. Ozfidan, M. Vladisavljevic, M. Korkusinski, and P. Hawrylak, *Electron-electron interactions, topological phase, and optical properties of a charged artificial benzene ring*, *Phys. Rev. B* **92** (Dec, 2015) 245304.

[49] M. Czyzyk and M. Podgorny, *Energy bands and optical properties of hgte and cdte calculated on the basis of the tight-binding model with spin-orbit interaction*, *Phys. Stat. Solidi. B* **98** (1980) 507.

[50] S. Mao, A. Yamakage, and Y. Kuramoto, *Tight-binding model for topological insulators: Analysis of helical surface modes over the whole brillouin zone*, *Phys. Rev. B* **84** (Sep, 2011) 115413.

[51] D. B. Topalović, V. V. Arsoski, M. Ž. Tadić, and F. M. Peeters, *Confined electron states in two-dimensional hgte in magnetic field: Quantum dot versus quantum ring behavior*, *Phys. Rev. B* **100** (Sep, 2019) 125304.

[52] L. Castro-Enriquez, L. Quezada, and A. Martín-Ruiz, *Optical response of a topological-insulator-quantum-dot hybrid interacting with a probe electric field*, *Physical Review A* **102** (2020), no. 1 013720.

[53] V. Kaladzhyan, P. P. Aseev, and S. N. Artemenko, *Photogalvanic effect in the hgte/cdte topological insulator due to edge-bulk optical transitions*, *Phys. Rev. B* **92** (Oct, 2015) 155424.

[54] L. Gioia, M. G. Christie, U. Zülicke, M. Governale, and A. J. Sneyd, *Spherical topological insulator nanoparticles: Quantum size effects and optical transitions*, *Phys. Rev. B* **100** (Nov, 2019) 205417.

[55] L. C. L. Y. Voon and M. Willatzen, *The kp method: electronic properties of semiconductors*. Springer Science & Business Media, 2009.

[56] E. O. Kane, *Energy band structure in p-type germanium and silicon*, *Journal of Physics and Chemistry of Solids* **1** (1956), no. 1-2 82–99.

[57] C. Kittel, *Introduction to solid state physics*. Wiley, 8 ed., 2021.

[58] B. Yan and S.-C. Zhang, *Topological materials*, *Reports on Progress in Physics* **75** (2012), no. 9 096501.

[59] M. Cygorek, M. Korkusinski, and P. Hawrylak, *Atomistic theory of electronic and optical properties of inasp/inp nanowire quantum dots*, *Phys. Rev. B* **101** (Feb, 2020) 075307.

[60] M. P. Marder, *Condensed matter physics*. John Wiley & Sons, 2 ed., 2010.

[61] K. v. Klitzing, G. Dorda, and M. Pepper, *New method for high-accuracy determination of the fine-structure constant based on quantized hall resistance*, *Phys. Rev. Lett.* **45** (Aug, 1980) 494–497.

[62] R. B. Laughlin, *Quantized hall conductivity in two dimensions*, *Phys. Rev. B* **23** (May, 1981) 5632–5633.

[63] R. B. Laughlin, *Anomalous quantum hall effect: An incompressible quantum fluid with fractionally charged excitations*, *Phys. Rev. Lett.* **50** (May, 1983) 1395–1398.

[64] J. Weis, *Quantum hall effect*, in *Encyclopedia of Condensed Matter Physics* (F. Bassani, G. L. Liedl, and P. Wyder, eds.), pp. 22–29. Elsevier, Oxford, 2005.

[65] X.-L. Qi and S.-C. Zhang, *Quantum spin hall effect and topological insulators*, *Physics Today* **63** (2010) 33.

[66] C. Day, *Quantum spin hall effect shows up in a quantum well insulator, just as predicted*, *Physics Today* **61** (2008), no. 1 19.

[67] F. D. M. Haldane, *Model for a quantum hall effect without landau levels: Condensed-matter realization of the "parity anomaly"*, *Phys. Rev. Lett.* **61** (Oct, 1988) 2015–2018.

[68] C. L. Kane and E. J. Mele, *Quantum spin hall effect in graphene*, *Physical review letters* **95** (2005), no. 22 226801.

[69] S. Murakami, N. Nagosa, and S.-C. Zhang, *Su (2) non-abelian holonomy and dissipationless spin current in semiconductors*, *Physical Review B* **69** (2004), no. 23 235206.

[70] J. Sinova, D. Culcer, Q. Niu, N. Sinitsyn, T. Jungwirth, and A. H. MacDonald, *Universal intrinsic spin hall effect*, *Physical review letters* **92** (2004), no. 12 126603.

[71] B. A. Bernevig and S.-C. Zhang, *Quantum spin hall effect*, *Phys. Rev. Lett.* **96** (Mar, 2006) 106802.

[72] J. Alicea, *New directions in the pursuit of majorana fermions in solid state systems*, *Reports on progress in physics* **75** (2012), no. 7 076501.

[73] R. Ashoori, *Electrons in artificial atoms*, *Nature* **379** (1996), no. 6564 413–419.

[74] C. R. Harris and et al., *Array programming with NumPy*, *Nature* **585** (Sept., 2020) 357–362.

[75] W. Trzeciakowski, *Boundary conditions and interface states in heterostructures*, *Phys. Rev. B* **38** (Aug, 1988) 4322–4325.

[76] W. Trzeciakowski, *Effective-mass approximation in semiconductor heterostructures: One-dimensional analysis*, *Phys. Rev. B* **38** (Dec, 1988) 12493–12507.

[77] M. J. Giuliodori, H. L. Lujan, W. S. Briggs, G. Palani, and S. E. DiCarlo, *Hooke's law: applications of a recurring principle*, *Advances in physiology education* **33** (2009), no. 4 293–296.

[78] C. Yuan, Y. Mei, A. Hong, T. Yu, Y. Yang, F. Zeng, K. Xu, Q. Li, X. Luo, J. He, et al., *Strain engineered band structure and optical properties of confined gaas quantum dots*, *The Journal of Physical Chemistry C* **121** (2017), no. 10 5800–5804.

[79] G. L. Bir and G. E. Pikus, *Symmetry and strain-induced effects in semiconductors*, vol. 484. Wiley New York, 1974.

[80] C. G. Van de Walle, *Band lineups and deformation potentials in the model-solid theory*, *Phys. Rev. B* **39** (Jan, 1989) 1871–1883.

[81] M. Planck, *On an improvement of wien's equation for the spectrum*, *Ann. Physik* **1** (1900) 719–721.

[82] P. A. M. Dirac, *The quantum theory of the emission and absorption of radiation*, *Proceedings of the Royal Society of London. Series A, Containing Papers of a Mathematical and Physical Character* **114** (1927), no. 767 243–265.

[83] E. Fermi, *Nuclear physics: a course given by Enrico Fermi at the University of Chicago*. University of Chicago Press, 1950.

[84] F. H. Faisal, *A theory of multiple photon absorption by graphene in intense laser fields*, *Annalen der Physik* **525** (2013), no. 1-2 171–179.

[85] L. Szulakowska, *Electron-electron Interactions and Optical Properties of Two-dimensional Nanocrystals*. PhD thesis, University of Ottawa, September, 2020.

[86] F. Wilczek, *A theoretical physicist examines exotic particles lurking in new materials*, *Nature* **458** (2009) 129.

[87] A. Y. Kitaev, *Fault-tolerant quantum computation by anyons*, *Annals of Physics* **303** (2003), no. 1 2–30.

[88] L. Fu and C. L. Kane, *Superconducting proximity effect and majorana fermions at the surface of a topological insulator*, *Phys. Rev. Lett.* **100** (Mar, 2008) 096407.

[89] X.-L. Qi, T. L. Hughes, and S.-C. Zhang, *Topological field theory of time-reversal invariant insulators*, *Physical Review B* **78** (2008), no. 19 195424.

[90] J. C. Slater and G. F. Koster, *Simplified lcao method for the periodic potential problem*, *Phys. Rev.* **94** (Jun, 1954) 1498–1524.

Appendix: HgTe parameters

Here we present the parameters of HgTe derived in Allan and Deleure's work [1] and used when calculating HgTe's bandstructure, Fig. 2.1 in section 2.1. HgTe has a $sp^3d^5s^*$ electronic configuration with the lattice parameter being $a = 6.453\mathring{A}$ [1].

Table A1: HgTe Slater and Koster [90] parameters. Δ is the spin-orbit coupling, (a) is the anion (Te), and (c) is the cation (Hg). E_s is, e.g., the s orbital energy and the zero of energy is taken at the top of the valence band. HgTe's d orbitals have two energy parameters but QNANO implements only one energy for all 5 d orbitals, thus we take the average of these values in QNANO.

HgTe Parameters (eV)			
$E_s(a)$	-10.040161	$E_s(c)(0K)$	-1.502103
$E_p(a)$	1.580003	$E_p(c)$	5.929255
$E_d(a)$	11.642677	$E_d(c)$	15.270032
$E_{s^*}(a)$	12.611213	$E^*_s(c)$	14.801158
$\Delta(a)$	0.375000	$\Delta(c)$	0.465000
$V_{ss\sigma}(ac)$	-0.904384	$V_{ss\sigma}(ca)$	-1.570513
$V_{ss^*\sigma}(ac)$	0.357261	$V_{ss^*\sigma}(ca)$	-0.242580
$V_{sp\sigma}(ac)$	1.085069	$V_{sp\sigma}(ca)$	2.014492
$V_{s^*p\sigma}(ac)$	1.175059	$V_{s^*p\sigma}(ca)$	1.405375
$V_{sd\sigma}(ac)$	-0.52896	$V_{sd\sigma}(ca)$	-1.067102
$V_{s^*d\sigma}(ac)$	0.485896	$V_{s^*d\sigma}(ca)$	0.696627
$V_{pp\sigma}(ac)$	3.166827	$V_{pp\sigma}(ca)$	-0.945694
$V_{pd\sigma}(ac)$	-1.789915	$V_{pd\sigma}(ca)$	-0.653612
$V_{pd\pi}(ac)$	1.406422	$V_{pd\pi}(ca)$	1.657517
$V_{pd\sigma}(ac)$	-0.529629	$V_{dd\pi}(ca)$	2.424709
$V_{pd\delta}(ac)$	-1.064207		